Title

Energetic Trade-Offs and Hypometabolic States Promote Disease Tolerance.

Journal

Cell, 177(2)

Authors

Ganeshan, Kirthana
Nikkanen, Joni
Man, Kevin
et al.

Publication Date

2019-04-04

DOI

10.1016/j.cell.2019.01.050

Peer reviewed

HHS Public Access

Author manuscript

Cell. Author manuscript; available in PMC 2020 April 04.

Published in final edited form as:

Cell. 2019 April 04; 177(2): 399–413.e12. doi:10.1016/j.cell.2019.01.050.

Energetic trade-offs and hypometabolic states promote disease tolerance

Kirthana Ganeshan[1,6], **Joni Nikkanen**[1,6], **Kevin Man**[1,6], **Yew Ann Leong**[1,2,6], **Yoshitaka Sogawa**[1], **J. Alan Maschek**[3,4], **Tyler Van Ry**[3,4], **D. Nyasha Chagwedera**[1], **James E. Cox**[3,4], and **Ajay Chawla**[1,5,7]

[1]Cardiovascular Research Institute, University of California, San Francisco, 94143-0795, USA

[2]Centre for Inflammatory Diseases, Department of Medicine, School of Clinical Sciences at Monash Health, Monash University, Australia

[3]Department of Biochemistry, University of Utah, Salt Lake City, UT 84112

[4]Metabolomics Core Research Facility, University of Utah, Salt Lake City, UT 84112

[5]Departments of Physiology and Medicine, University of California, San Francisco, 94143-0795, USA

[6]These authors contributed equally to this work

[7]Lead contact

Summary

Host defenses against pathogens are energetically expensive, leading ecological immunologists to postulate that they might participate in energetic trade-offs with other maintenance programs. However, the metabolic costs of immunity and the nature of physiologic trade-offs it engages are largely unknown. We report here that activation of immunity causes an energetic trade-off with the homeothermy (the stable maintenance of core temperature), resulting in hypometabolism and hypothermia. This immunity-induced physiologic trade-off was independent of sickness behaviors but required hematopoietic sensing of lipopolysaccharide (LPS) via the toll-like receptor 4 (TLR4). Metabolomics and genome-wide expression profiling revealed that distinct metabolic programs supported entry and recovery from the energy conserving hypometabolic state. During bacterial infections, hypometabolic states, which could be elicited by competition for energy between maintenance programs or energy restriction, promoted disease tolerance. Together, our

Correspondence: ajay.chawla@ucsf.edu (A.C.).

Author Contribution

K.G., J.N., K.M., Y.A.L., and Y.S. designed and performed the main experiments. J.A.M, T.V.R, and J.E.C. quantified acylcarnitines in plasma and liver. K.G., J. N., K.M., Y.A.L., Y.S., and A.C. conceived, discussed, interpreted the results, and wrote the paper.

The authors declare that they have no competing financial interests.

DATA AND SOFTWARE AVAILABILITY

The RNA-seq data has been deposited at GEO (https://www.ncbi.nlm.nih.gov/geo/) under the accession number GEO: GSE114473.

findings suggest that energy conserving hypometabolic states, such as dormancy, might have evolved as a mechanism of tissue tolerance.

Graphical Abstract

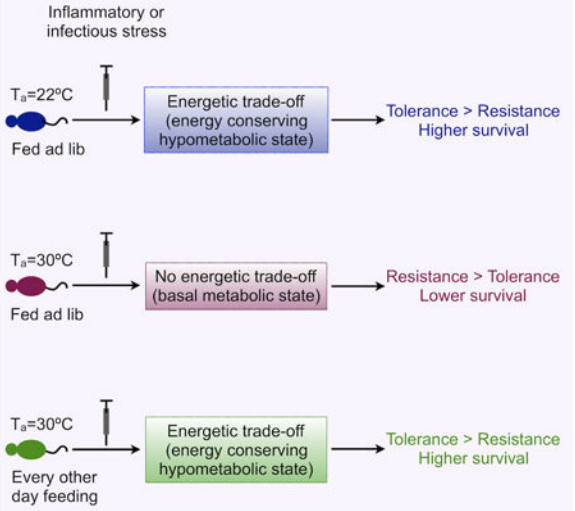

In Brief

Immune activation after infection is metabolically costly, competing for energy with the maintenance of normal body temperature, and this dynamic trade-off leads to preferential use of tolerance as a mechanism of bacterial defense.

Introduction

Immunity, a high cost-high benefit trait, protects against infections and injury (Lochmiller and Deerenberg, 2000; Sadd and Schmid-Hempel, 2009; Zuk and Stoehr, 2002). In addition to collateral damage and immunopathology, the activation of immunity poses a significant metabolic challenge for the host (Lochmiller and Deerenberg, 2000; Odegaard and Chawla, 2013; Sadd and Schmid-Hempel, 2009). For example, pathogen-directed inflammatory responses, which include production of inflammatory mediators, respiratory burst, acute phase response, cellular migration, and cellular proliferation, are energetically expensive, necessitating the reallocation of nutrients (glucose, amino acids, and fatty acids) to fuel immune activation (Ganeshan and Chawla, 2014; O'Neill and Pearce, 2016; Thompson, 2011). Moreover, because sickness behavior of anorexia accompanies infections, mobilization of stored fuels is critical for survival (Lochmiller and Deerenberg, 2000; Wang et al., 2016). Peripheral insulin resistance, which decreases nutrient storage in muscle, fat, and liver, provides one mechanism for prioritization and reallocation of metabolic fuels for host defense (Odegaard and Chawla, 2013). Because the metabolic costs of immunity are high (Lochmiller and Deerenberg, 2000; Sadd and Schmid-Hempel, 2009), it is likely that immunity competes with other host maintenance programs for energy. However, the nature of this competition and the physiologic trade-offs they might promote remain poorly understood.

The host response to a pathogen is dictated by a number of factors, including the severity, type, and duration of infection, and the location, virulence, and replication status of the pathogen. The innate immune system uses cell surface and intracellular pattern-recognition receptors to sense pathogens (Tan and Kagan, 2014). The information gathered from these sensors allows the immune system to gauge the nature of the threat (viral, bacterial, fungal), its location (extracellular, intracellular), its replication status, and severity. These inputs are integrated into effector responses, which aim to eliminate, neutralize, or contain the microbial pathogen. The types of effector responses and their order of deployment is further optimized to minimize costs (metabolic and immunopathology) while providing sufficient protection against the pathogen (Sadd and Schmid-Hempel, 2009; Zuk and Stoehr, 2002).

Infected hosts can protect themselves using two different defense strategies (Ayres and Schneider, 2012; Medzhitov et al., 2012; Raberg et al., 2009; Soares et al., 2017). First, they can use resistance to attack pathogens, resulting in reduction of pathogen burden. Second, they can employ tolerance to limit damage caused by the pathogen and the host immune response. While these two defense strategies had been recognized in the field of plant ecology for decades (Simms and Triplett, 1994), the concept of tissue tolerance was only recently introduced into animal studies (Ayres and Schneider, 2008; Jamieson et al., 2013; Raberg et al., 2007; Schieber et al., 2015; Torres et al., 2016; Wang et al., 2016; Weis et al., 2017). As such, the overarching principles and mechanisms that control expression of tissue tolerance programs remain largely unknown. However, recent studies suggest that metabolic adaptations to bacterial infections are a critical determinant of tissue tolerance (Wang et al., 2016; Weis et al., 2017).

Here, we investigated whether the need and competition for energy might be an additional determinant of the type of defense an animal uses against pathogens. We tested this idea by activating the energy intensive trait of immunity in mice, who had a competing need for energy to maintain homeothermy. We found that activation of immunity by a number of TLR ligands promoted sickness behaviors of anorexia and lethargy, whereas energetic trade-off with homeothermy was preferentially induced by the TLR4 ligand lipopolysaccharide (LPS). Using LPS-activated immunity as a model, we uncovered the mechanisms by which immunity initiates physiologic trade-offs with homeothermy. Application of these findings revealed that hypometabolic states, elicited by energetic competition or energy restriction, promoted tolerance during bacterial infections.

Results

Activation of immunity by LPS triggers energy conservation

Organisms acquire energy from their environment, which they allocate to growth, reproduction, and maintenance (Stearns, 1992). In the laboratory setting, basal tissue homeostasis (basal metabolic rate, BMR), activity (locomotor activity), and adaptive thermogenesis (homeothermy) are the major energy consuming maintenance programs in adult nonreproductive mice. To model competition for energy between these maintenance programs and immunity, we treated mice with various TLR ligands because they provide an interpretable system to interrogate host-derived responses. Our experimental paradigm consisted of housing mice at the normal vivarium temperature (22°C), a temperature that is

below their thermoneutral zone (Cannon and Nedergaard, 2011; Ganeshan and Chawla, 2017), and monitoring changes in various physiologic parameters after activation of immunity. By performing a systematic screen with ligands for TLRs 1–5, 7/8, and 9, we found that the TLR4 ligand LPS had the strongest effect on energy conservation (i.e. reduction in oxygen consumption, VO_2), which occurred in a dose-dependent manner (Figure 1A, B, and S1A, D, G, J, and S2A). In contrast, sickness behaviors of anorexia and lethargy were observed in mice administered ligands for TLRs 1–5 (Figure 1A, S1B, C, E, F, H, I, K, L, and S2B, C).

To study how competition for energy between immunity and other maintenance programs initiates physiologic trade-offs, we repeated the experiments with LPS using mice housed at different ambient temperatures (T_a). At thermoneutrality (T_a=30°C), mice do not expend any additional energy for homeothermy, whereas at the normal vivarium temperature of 22°C mice depend on adaptive thermogenesis to maintain their core temperature (Cannon and Nedergaard, 2011; Ganeshan and Chawla, 2017). While treatment with LPS decreased VO_2 in both groups of mice, the mechanisms for and the phenotypes resulting from this energy savings were distinct (Figure 1C, D). In thermoneutral mice, the ~35% reduction in oxygen consumption was achieved by suppression of locomotor activity during the dark cycle (Figure 1C, E). Because oxygen consumption did not drop below the BMR in these animals (Figure 1C, red dashed line), it suggests that energy savings from inhibition of locomotor activity were sufficient to fuel immune activation. In contrast, mice housed at 22°C decreased their VO_2 by ~52% (Figure 1D). The energy savings in this case were achieved by reducing expenditure on all three maintenance programs: locomotor activity, BMR, and homeothermy (Figure 1D, F). As a consequence, animals housed at 22°C abandoned homeothermy and decreased their core body temperature, whereas the core temperature of thermoneutral mice did not drop below 35°C after administration of LPS (Figure 1G). Infrared imaging revealed a similar decrease in dorsal surface temperature of these animals (Figure 1H, I). These observed differences in strategies of energy conservation were independent of sickness behaviors of anorexia and lethargy, which were present in both groups of mice (Figure 1E, F, J, K). LPS-induced energy conservation was also independent of changes in the respiratory exchange ratio (Figure S2D, E), and circulating levels of glucose and leptin (Fig. 1L, M). Because activation of innate immunity by LPS is primarily fueled by glycolytic rather than oxidative metabolism (Ganeshan and Chawla, 2014; O'Neill and Pearce, 2016), our findings suggest that the host monitors metabolic costs associated with innate immune activation, rather than fuel preference, to direct physiologic tradeoffs between maintenance programs.

Hematopoietic-endothelial sensing of LPS triggers energy conservation but not sickness behaviors

To understand the underlying mechanisms, we began by asking how LPS is sensed to promote the energetic trade-off with homeothermy. Cell surface TLR4 and the adaptor protein Myeloid Differentiation Primary Response 88 (MyD88) sense extracellular LPS to initiate inflammatory responses (Tan and Kagan, 2014), whereas intracellular LPS activates Caspase 11 in a TLR4-independent manner to initiate pyroptosis (Hagar et al., 2013; Kayagaki et al., 2013). We found that *Tlr4*$^{-/-}$ and *Myd88*$^{-/-}$ mice did not engage in sickness

behaviors or physiologic trade-off with homeothermy (Figure 2A-D, S2F-K), indicating that LPS-induced energy conservation and sickness behaviors are initiated by sensing of extracellular LPS.

We next asked what cells sense LPS to initiate energy conservation and sickness behaviors. At site of LPS injection, we found that TLR4 was expressed by peritoneal macrophages, $CD11c^+$ cells, and to a lesser extent by B1a cells (Figure S3A-C). To test whether myeloid cells were the primary sensors of LPS for entry into the hypometabolic state, we deleted *Tlr4* or *Myd88* in myeloid cells using $Lyz2^{Cre}$ mice. Although the rate of entry, depth, and duration of the hypometabolic state was reduced in $Tlr4^{f/f}Lyz2^{Cre}$ and $Myd88^{f/f}Lyz2^{Cre}$ mice (Figure 2E, F and S3D-G), these animals still responded to LPS by decreasing their metabolic rate. These findings suggested that either $Lyz2^{Cre}$-mediated deletion was incomplete (Abram et al., 2014) or additional cells, such as the $CD11c^+$ or B1a cells, can sense LPS to trigger energy conservation. To address this question, we used $Vav1^{Cre}$ to delete *Tlr4* or *Myd88* in all hematopoietic and endothelial cells (Abram et al., 2014). Unlike $Tlr4^{f/f}Lyz2^{Cre}$ and $Myd88^{f/f}Lyz2^{Cre}$ mice, $Tlr4^{f/f}Vav1^{Cre}$ and $Myd88^{f/f}Vav1^{Cre}$ mice did not decrease their VO_2 below the resting metabolic rate (RMR, designated by the red dashed line in Figure 2G, H) or abandon homeothermy (Figure S3H, I) in response to LPS, suggesting that when immunity is not directly activated by the LPS-TLR4-MyD88 signaling pathway, its metabolic costs are low and a trade-off with homeothermy is unnecessary. However, $Tlr4^{f/f}Vav1^{Cre}$ and $Myd88^{f/f}Vav1^{Cre}$ mice still responded to LPS by engaging in sickness behaviors, as evidenced by reduction in locomotor activity, food intake, and body mass (Figure 2I-L and S3J, K). Taken together, these data suggest that hematopoietic-endothelial sensing of LPS is required for entry into the hypometabolic-hypothermic state, whereas sensing of LPS in non-hematopoietic cells, such as stromal and parenchymal cells, is sufficient to promote sickness behaviors of lethargy and anorexia.

Shift in core set point and the Q_{10} effect suppress metabolic rate

We next asked what mechanisms lower metabolic rate to promote energy conservation. To address this question, we quantified changes in the assembly and activity of respiratory supercomplexes (RSCs), which dynamically regulate oxygen consumption by the respiratory chain (Garaude et al., 2016). We found that treatment of mice with LPS did not significantly alter the assembly or activity of complex I (CI, NADH:ubiquinone oxidoreductase)- and complex IV (CIV, cytochrome c oxidase)-containing RSCs in liver, brown adipose tissue (BAT), and heart of mice housed at 22°C and 30°C (Figure 3A–C). In addition, expression of complex II (CII, succinate dehydrogenase), complex V (CV, ATP synthase), and complex III (CIII, ubiquinol-cytochrome c oxidoreductase)-containing RSCs was not significantly different in livers and hearts of these animals (Figure 3A, C). Congruent with these observations, oxygen consumption rates were not reduced in isolated tissues (liver, BAT, and heart) as animals lowered their metabolic rate (Figure S4A-C). These results suggest that dynamic changes in RSCs or mitochondrial respiration do not account for suppression of metabolic rate by LPS.

Q_{10} effect of temperature on biochemical reactions is an alternative mechanism for lowering metabolic rate. The Q_{10} coefficient is a measure of how chemical or biochemical reactions

change with temperature. For example, a Q_{10} value of 2 indicates that the rate of biochemical reactions will increase or decrease by 2-fold for a 10°C increase or decrease in temperature, respectively. Since small heterotherms rely on the Q_{10} effect of temperature to lower their metabolic rate during daily torpor (Geiser, 2004), we asked whether this mechanism also suppresses metabolic respiration in LPS-treated mice. Using parameters from basal (VO_2=36 ml/hr and core temperature=36.1°C from Figs. 1C, G) and hypometabolic state (VO_2=17.5 ml/hr and core temperature=27.6°C from Figs. 1D, G), the calculated Q_{10} value for C57BL/6J mice stimulated with LPS was ~2.3. Because this Q_{10} value is similar to that of mice (Q_{10} of 2.4) and small heterotherms during torpor (Geiser, 2004; Tucker, 1962), it suggests that temperature-dependent mechanisms likely suppress metabolic rate to below BMR in animals treated with LPS. In this model, LPS induces the hypometabolic state by decreasing the central set point for core temperature, which causes the metabolic rate to decrease from the higher RMR (measured at 22°C) to the lower BMR (measured at 30°C) (Figure 3D). As a consequence of this ~50% reduction in metabolic rate, the core temperature decreases, which causes an additional ~25% reduction in metabolic rate by the Q_{10} effect of temperature, resulting in the ~75% reduction in VO_2 observed in mice treated with LPS at 22°C (Figure 3D and 1D).

Relative metabolic costs of immunity trigger physiologic trade-off with homeothermy

Although an activated immune response has been postulated to be metabolically expensive (Lochmiller and Deerenberg, 2000; Sadd and Schmid-Hempel, 2009; Zuk and Stoehr, 2002), its energetic costs have not been systematically quantified. To address this question, we first quantified the energetic requirements of various maintenance programs over a 24-hour period. We found that, in thermoneutral mice (T_a=30°C), BMR consumed ~67% (2243 ml of VO_2) of energy with the remainder being spent on locomotor activity (~33%; 1123 ml of VO_2) (Figure 3E, F). In contrast, mice housed at 22°C spent ~37% (2243 ml of VO_2) on BMR, ~15% (898 ml of VO_2) on locomotor activity, and ~48% (2933 ml of VO_2) on adaptive thermogenesis (Figure 3E, F). We next calculated immunity-associated energy savings in mice housed at 22°C and 30°C. In thermoneutral mice, immune activation by LPS resulted in absolute energy savings of 1170 ml of VO_2 from loss of locomotor activity (Figure 3G), whereas energy savings were ~2.7-fold higher in absolute terms (3182 ml of VO_2) in mice housed at 22°C, which resulted from combined reductions in locomotor activity, adaptive thermogenesis, and BMR (Figure 3G).

There are two possible reasons for the higher energy savings observed in mice housed at 22°C. First, since the metabolic costs of immunity are proportional to the elicited inflammatory response (Lochmiller and Deerenberg, 2000), the innate immune response might be higher in mice housed at 22°C. Second, relative rather than absolute costs serve as the trigger for the physiologic trade-off and energy conservation. To distinguish between these two possibilities, we quantified the inflammatory response induced by LPS in mice housed at 22°C and 30°C. We found that, irrespective of their housing temperature, LPS increased secretion of pro- and anti-inflammatory cytokines to a similar extent in these animals (Figure 3H and S4D-I). These data suggested that relative, rather than absolute, metabolic costs of immunity likely initiate the physiologic trade-off with homeothermy. In agreement with this postulate, the relative energy savings were comparable between the two

groups of mice (~52% at T_a=22°C vs. ~35% at T_a=30°C), especially when the suppressive effect of Q_{10} on metabolic rate (which accounts for 33%) was factored in (Figure 3I).

Activation of immunity reprograms nutrient metabolism in the liver

We next investigated how the host meets the competing metabolic demands of the various maintenance programs during immune activation. Because LPS-induced sickness behaviors decreased food intake, it resulted in a substrate shift from ingested carbohydrates to ketone bodies in both groups of mice (Figure 4A). Oxidation of fatty acids and amino acids, which are mobilized from white adipose tissue and skeletal muscle, respectively, supports ketogenesis in the liver. To gain insights into this process, we analyzed body composition of mice before and after administration of LPS. We found that both groups of mice lost weight, which was primarily due to a decrease in their lean body mass (Figure 4B). These observations suggested that immune activation by LPS mobilizes amino acids from skeletal muscle, which can then be used for catabolic or anabolic purposes. Indeed, expression and activity of ubiquitin ligases (*MuRF1* and *Atrogin1*), which are involved in the breakdown of intracellular proteins into amino acids (Bodine et al., 2001), were induced in the muscle (Figure S5A, B).

Liver has a critical role in supplying energy to peripheral tissues during fed and fasted states. To understand the mechanisms by which immunity reprograms liver metabolism, we performed RNA-seq at various time points after injection of LPS. Principle component analysis (PCA) revealed that variance in PCA1 (51.4%) and PCA2 (27.3%) reflected effects of LPS and ambient temperature, respectively (Figure S5C). However, to our surprise, LPS-induced changes in hepatic gene expression followed similar paths in both groups of mice (Figure S5C, D). We thus performed pathway analysis on genes that were differentially expressed at 12 hours in mice housed at 30°C. We found that pathways associated with inflammatory response, host defense, cytokine production, and LPS signaling were enriched amongst the induced genes (Figure S5E, F), whereas gene ontologies associated with fatty acid metabolism, drug and xenobiotic metabolism, amino acid metabolism, and PPAR signaling were suppressed (Figure 4C).

During fasting, PPARα induces genes involved in β-oxidation of fatty acids and ketogenesis (Rakhshandehroo et al., 2010). However, we found that nearly the entire program of fatty acid catabolism, including the PPARα targets in mitochondrial β-oxidation and peroxisomal fatty acid oxidation, was suppressed (Figure 4D), suggesting that oxidation of fatty acids might not be the primary means of supporting ketogenesis during LPS-induced anorexia. We tested this hypothesis by quantifying acylcarnitines in plasma and liver, which are elevated when oxidation of fatty acids or amino acids is impaired. For instance, elevation of C2–C5 carnitines suggests defects in oxidation of short chain fatty acids or amino acids, whereas increases in C6–C18 carnitines is clinically diagnostic of defects in oxidation of medium- and long-chain fatty acids (Knottnerus et al., 2018). Congruent with the RNA-seq data, LC-MS analysis of acylcarnitines in plasma and liver revealed a general impairment in oxidation of medium- and long-chain fatty acids. For example, nearly all of the medium- and long-chain acylcarnitines (C6–C20) were increased in plasma of thermoneutral mice after administration of LPS (Figure 4E and Table S1). This global increase in plasma

acylcarnitines was accompanied by ~3.4-fold decrease in plasma free carnitine (C0), suggesting increased utilization of carnitine for the production of acylcarnitines (Figure 4E and Table S1). Indeed, quantification of acylcarnitines in the liver revealed accumulation of free carnitine and higher levels of medium- and long-chain acylcarnitines (Figure 4F and Table S1). Quantitative RT-PCR analysis further confirmed that genes important in production of acylcarnitines (*Cpt1a*, *Cpt1b*, and *Slc22a5* (carnitine transporter)) were induced, whereas expression of mitochondrial carnitine-acylcarnitine translocase (*Slc25a20*), which translocates acylcarnitines into the inner mitochondrial matrix for β-oxidation, was suppressed in livers of thermoneutral mice (Figure S5G). A similar increase in medium- and long-chain acylcarnitines was observed in plasma and liver of mice housed at 22°C after treatment with LPS (Figure S5H, I and Table S1). These findings indicate that LPS-induced inflammation disrupts the normal homeostatic response to fasting by suppressing the PPARα-regulated mitochondrial and peroxisomal oxidation of fatty acids. In support of this postulate, plasma metabolomics revealed accumulation of medium-, long-, and very long-chain fatty acids in both groups of mice (Figure 4G).

In addition to fatty acids, amino acids can serve as substrates for synthesis of ketone bodies (Noda and Ichihara, 1976). The entry of amino acids into the ketogenic pathway is schematically shown in Figure 4H. RNA-seq analysis revealed that pathways controlling the catabolism of ketogenic amino acids were dynamically regulated in livers of mice treated with LPS (Figure 4I). For example, while genes important in catabolism of lysine and tyrosine were unchanged or induced in both groups of mice, those controlling the degradation of leucine, isoleucine, and tryptophan exhibited greater variation in their expression. These findings suggested that not all ketogenic amino acids are equally catabolized during LPS-induced anorexia. Indeed, metabolomics revealed that circulating levels of lysine and tyrosine declined rapidly in both groups of mice, whereas phenylalanine remained unchanged (Figure 4L and Table S2). In addition, the reduction in plasma levels of leucine, isoleucine, and tryptophan temporally mirrored the expression profiles of their catabolic enzymes (Figure 4I, J). Together, these observations suggest that immune activation by LPS reprograms liver metabolism to favor catabolism of amino acids over fatty acids to support ketogenesis. In support of this substrate shift, production of urea was increased in the liver and plasma, thus confirming increased catabolism of amino acids (Figure 4K and S5J).

Thermogenesis in BAT supports recovery from hypometabolic-hypothermic state

Brown adipose tissue (BAT)-mediated thermogenesis provides a defense against environmental cold in mammals (Cannon and Nedergaard, 2011; Harms and Seale, 2013). Although BAT can use glucose and fatty acids to support thermogenesis, plasma triglycerides preferentially fuel cold-induced thermogenesis (Bartelt et al., 2011; Dijk et al., 2015). For example, in hypertriglycerdemic *Apoa5*$^{-/-}$ mice, cold exposure activates BAT thermogenesis to accelerate the clearance of plasma triglycerides (Bartelt et al., 2011). We got a hint that this might also be the case for exiting from LPS-induced hypometabolic-hypothermic state, because plasma metabolomics revealed an increase in triglycerides at 24 hours in mice housed at 30°C (Figure 5A and Table S3), which did not develop hypothermia. Visual inspection of plasma confirmed lipemia (Figure 5B), which was secondary to

transient hypertriglyceridemia in these animals (Figure S6A). We next asked whether increased synthesis of triglycerides in the liver or their impaired clearance in the periphery contributed to the observed hypertriglyceridemia. Although livers of mice housed at 30°C were steatotic 24 hours after administration of LPS (Figure S6B, C), the expression of the lipogenic transcription factor *Srebf1* and its target genes (*Fasn*, *Scd1*, and *Acaca*) was suppressed (Figure 5C), indicating impaired clearance of triglycerides in these animals. We tested this hypothesis by quantifying levels of ANGPTL4, a potent inhibitor of lipoprotein lipase and triglyceride clearance (Dijk et al., 2015). We found that circulating levels of ANGPTL4 were higher in plasma of mice at 30°C (Figure 5D). To determine whether ANGPTL4 contributes to impaired triglyceride clearance in mice housed at 30°C, we quantified plasma triglycerides in C57BL/6J and $Angptl4^{-/-}$ mice 24 hours after injection with LPS. We observed that plasma triglycerides were reduced in $Angptl4^{-/-}$ mice housed at 30°C (Figure 5E), indicating that impaired clearance, rather than increased synthesis, contributes to triglyceride accumulation in these animals.

Uncoupling protein 1 (UCP1) is required for BAT thermogenesis (Harms and Seale, 2013), prompting us to ask whether heat production in BAT might be necessary for exiting from the hypometabolic-hypothermic state. Indeed, unlike C57BL/6J mice, $Ucp1^{-/-}$ mice failed to increase their metabolic rate (Figure 5F and S6D-G), resulting in persistent hypothermia and tissue dysfunction, as evidenced by increases in biomarkers of kidney (creatinine), heart (troponin), and skeletal and cardiac muscles (creatine kinase) damage (Figure 5G-J). This worsening of organ function was independent of the acute inflammatory response, which was similar in both groups of mice (Figure 5K and S6H–M). Furthermore, the inability to exit from the hypothermic-hypometabolic state decreased survival of $Ucp1^{-/-}$ mice housed at 22°C but not in those at 30°C, an ambient temperature at which UCP1-mediated thermogenesis is unnecessary (Figure 5F, L). In sum, these results suggest that fatty acid fueled uncoupled respiration in brown fat supports the exit from the LPS-induced hypometabolic state, and failure to exit from this hypothermic state causes tissue damage and decreases survival independent of the acute inflammatory response.

Competition for energy directs host defense strategies

Because immunity competes for energy with homeothermy, we next asked whether competition for energy affects the defense strategy (resistance vs. tolerance) a host uses against pathogens. We tested this hypothesis using two different models of infections, *L. monocytogenes* and *E. coli*. Infection with *L. monocytogenes* promoted anorexia (Figure 6A), resulting in weight loss in both groups of mice (Figure 6B). However, the severity of anorexia and weight loss were significantly attenuated in mice housed at 22°C (Figure 6A, B). Since these differences in body weight were independent of the inflammatory/febrile responses and liver bacterial burden (Figure 6C, D and S7A-B), we asked whether they might reflect intrinsic differences in tissue tolerance. To test this idea, we plotted host fitness against liver bacterial burden and found that mice housed at 22°C were more tolerant (Figure 6E), as evidenced by their lower slope on the reaction norm plot (Raberg et al., 2007).

Previous studies in flies suggest that utilization of resistance or tolerance is microbe-specific (Ayres and Schneider, 2008), leading us to ask whether competition for energy regulates

plasticity in host defense strategies against other pathogens. By infecting mice with *E. coli*, we found that the sickness behaviors of fever and anorexia were induced in both groups of mice (Figure 6F and S7C). Although host health (as assessed by weight loss) was not significantly different between the two groups (Figure 6F), livers and spleens of mice housed at 22°C had higher bacterial burden (Figure 6G, H), which was independent of tissue mass (Figure S7D, E). Similar to the metabolic adaptations observed with LPS, infection with *E. coli* led to increases in plasma triglycerides and ketone bodies in mice housed at 30°C (Figure 6I and S7F). Since the systemic inflammatory response to *E. coli* was similar between the two groups (Figure 6J), it suggests that mice housed at 22°C can tolerate higher pathogen burden in their tissues. Consistent with this hypothesis, infection with a higher inoculum of *E. coli* resulted an energetic trade-off with homeothermy and a lower mortality rate in mice housed at 22°C (Figure S7G and 6K, L). A similar survival benefit was observed in mice housed at 22°C that were administered a higher dose of LPS (Figure S7H). Altogether, these findings demonstrate that the host response to pathogens is highly plastic and competition for energy between maintenance programs is a determinant of whether the host employs tolerance, in addition to resistance, as a defense against pathogens.

We next asked whether timely exit from the hypothermia-hypometabolic state is required for maintenance of tissue tolerance during infection. We found that tissue pathogen burden was similar in wild type and *Ucp1*$^{-/-}$ mice infected with 1×10^7 CFU of *E. coli* (Figure 6M, N). However, infection with a higher inoculum of *E. coli* (1×10^8 CFU) resulted in increased mortality in *Ucp1*$^{-/-}$ mice (Figure 6O), which was likely secondary to persistent hypothermia (Figure 6P). In aggregate, these findings indicate that UCP1 is required for maintenance of tissue tolerance during immune activation by LPS or infection by *E. coli*.

Energy conserving hypometabolic state promotes tolerance during bacterial infection

Mammals conserve energy during the dormant state of torpor, which can be mimicked in the laboratory setting by fasting (Melvin and Andrews, 2009). We thus asked whether every other day fasting (EODF) could elicit prolonged energy conservation to promote tolerance in mice. To test this hypothesis, we housed mice at thermoneutrality (T_a=30ºC), an ambient temperature at which they are less tolerant, and subjected them to EODF. We found that when C57BL/6J female mice were subjected to 5 cycles of EODF, they lost body mass during the fasting days but gained it back during the fed days (Figure 7A). This stability in body mass resulted from energy conservation and hyperphagia (Figure 7B and S7I). For example, compared to *ad libitum* controls, EODF mice conserved energy on both fasted (~44% reduction in VO_2) and fed (~23% reduction in VO_2) days (Figure 7B-D), and increased their food intake by ~45% on fed days (Figure S6I). This dramatic reduction in metabolic rate was accompanied by a modest decrease (~1.5ºC) in core temperature (Figure 7E), which likely resulted from a decrease in locomotor activity (Figure 7F–H).

Because mice subjected to EODF conserved energy but maintained homeothermy, it provided us with a model to ask whether energy conservation was sufficient to enhance disease tolerance. For these experiments, mice were fed *ad libitum* or subjected to 5 cycles of EODF, and infected with *E. coli* upon completion of their last feeding cycle when their body weights were similar (Figure 7A). Compared to their *ad libitum* fed controls, EODF

mice recovered faster from infection-induced weight loss and hypothermia, and had reduced mortality after infection with 1×10^7 CFU *E. coli* (Figure 7I–K). Furthermore, at higher inoculum of *E. coli* (1×10^8 CFU), we observed a bigger difference in the survival rate, but not tissue bacterial burden, of *ad libitum* fed and EODF mice (Figure 7L and S7J, K). Taken together, these results demonstrate that energy conserving hypometabolic states, rather than hypothermia, promote tissue tolerance during bacterial infections.

Discussion

Life history theory postulates that limited resources are available for investment in growth, reproduction, and maintenance, necessitating trade-offs amongst these life history traits (Stearns, 1992). Since immunity enhances organismal fitness, it has been postulated to engage in trade-offs with other life history traits (McDade, 2005; Rauw, 2012). Experimental and empirical studies provide some support for this hypothesis. For example, transgenic expression of interleukin-6 (IL-6) in mice reduces circulating levels of insulin-like growth factor-1 (IGF-1), resulting in lower growth rate and smaller body size (De Benedetti et al., 1997). These inhibitory effects of IL-6 on growth can be partially reversed by neutralization of IL-6, suggesting that chronic inflammation can promote a trade-off with growth. In a similar manner, activation of *Toll* signaling pathway in the fat body of *D. melanogaster* suppresses insulin signaling, leading to a decrease in nutrient storage and growth (DiAngelo et al., 2009). Conversely, studies in livestock and meat-producing animals suggest that suppression of immune activation can enhance growth. For example, supplementation of animal feed with antibiotics enhances growth performance in chicken, guinea fowl, swine, and cattle (Dibner and Richards, 2005; Lochmiller and Deerenberg, 2000). In part, these growth-promoting effects of antibiotics have been attributed to suppression of immune activation by commensal and pathogenic microbes in animals raised under unsanitary conditions (Dibner and Richards, 2005; Lochmiller and Deerenberg, 2000). While these types of studies provide some evidence for immunity-associated trade-offs, the cumulative evidence is correlative, indirect, and does not address the underlying mechanisms.

Using TLR ligands, we found that activation of TLR4 signaling by LPS initiated an energetic trade-off with homeothermy in animals that had a competing demand for energy to maintain their body temperature. Three independent lines of evidence suggest that this energetic trade-off was likely triggered by the metabolic costs of immunity rather than sickness behaviors. First, LPS- and *E. coli*-induced physiologic trade-off occurred in a dose-dependent manner, demonstrating proportionality to the elicited immune response and its associated metabolic costs. Second, when LPS did not directly activate immunity in hematopoietic cells, as in $Tlr4^{f/f}Vav1^{Cre}$ and $Myd88^{f/f}Vav1^{Cre}$ mice, a metabolic trade-off with homeothermy did not occur. Third, LPS-induced sickness behaviors of anorexia and lethargy occurred in mice that did not engage in energetic trade-offs, such as animals housed at 30°C or $Tlr4^{f/f}Vav1^{Cre}$ and $Myd88^{f/f}Vav1^{Cre}$ mice. These findings collectively suggest that the host monitors and compares the metabolic costs of immunity against other maintenance programs, and whenever these costs exceed the available resources, a trade-off is triggered.

The energetic demands of immunity and its trade-off with homeothermy pose three significant metabolic challenges for the host. First, immune activation is associated with the sickness behavior of anorexia, which limits food intake and shifts reliance to stored nutrients, such as fatty acids and amino acids. Second, an effective immune response requires synthesis of many new proteins, including cytokines, chemokines, and acute phase reactants (Lochmiller and Deerenberg, 2000; Reeds and Jahoor, 2001). In the setting of anorexia, this increased demand for protein synthesis is likely met by mobilization of amino acids from skeletal muscle. Third, the recovery from the hypometabolic-hypothermic state is energetically expensive and requires thermogenesis in BAT, which is primarily fueled by fatty acids (Bartelt et al., 2011; Dijk et al., 2015).

Our findings suggest that the LPS-induced inflammatory response reprograms peripheral metabolism in multiple ways to support these new metabolic priorities. First, the inflammatory response induces expression of ubiquitin ligases *MuRF1* and *Atrogin1* to promote mobilization of amino acids from skeletal muscle, which can then be used for anabolic and catabolic functions. Second, LPS-induced inflammation suppresses PPARα-regulated fatty acid oxidation in the liver, as evidenced by accumulation of acylcarnitines in plasma and liver. This shifts reliance from fatty acid to amino acid oxidation to generate acetyl-coA, which is necessary for ketogenesis. However, it should be noted that PPARα is still required for the ketogenic response because it regulates the expression of mitochondrial HMG-CoA synthase, the rate-limiting step in ketone body production (Rakhshandehroo et al., 2010; Wang et al., 2016). Third, triglycerides and fatty acid-derived acylcarnitines provide substrates to fuel BAT thermogenesis (Bartelt et al., 2011; Simcox et al., 2017), allowing for timely exit from the hypometabolic-hypothermic state. Because these changes in nutrient mobilization and metabolism were observed in both euthermic and hypothermic mice, it suggests that the inflammatory response is antagonistic to normal homoeostatic programs irrespective of whether an energetic trade-off is elicited with homeothermy. Thus, the reprogramming of peripheral nutrient metabolism prepares the animal for a potential physiologic trade-off with homeothermy, but the decision to reduce metabolic rate and core temperature is likely made in the hypothalamus, where competing metabolic demands of the various maintenance programs are integrated by unclear mechanisms.

Resistance and tolerance enhance host fitness by two distinct mechanisms. While resistance relies on the immune system to clear pathogens, tolerance mechanisms involve both immune and non-immune cells, and act primarily on host health without affecting pathogen burden (Ayres and Schneider, 2012; Medzhitov et al., 2012; Raberg et al., 2009; Soares et al., 2017). Here, we demonstrated that energy conserving hypometabolic states favor utilization of tissue tolerance as a defense against bacterial pathogens. First, we found that competition for energy between immunity and homeothermy triggered entry into a hypometabolic-hypothermic state that enhanced tissue tolerance. Since this hypometabolic-hypothermic state resembles torpor, a strategy utilized by daily heterotherms to conserve energy during environmental hardships (Melvin and Andrews, 2009), it suggests co-evolution of tissue tolerance mechanisms with energy conserving traits. Indeed, in the second model, which used EODF to elicit energy conservation, hypometabolism without hypothermia was sufficient to enhance tolerance to bacterial infections. Because energy conservation preceded

infection in this model, it suggests that a regulated decrease in metabolic demand is critical for expression of tissue tolerance.

Our findings also have potential implications for humans. For example, targeted hypothermia is clinically being explored in humans to enhance survival in acutely ill patients, such as after myocardial infarction, stroke, or trauma. Although the initial clinical studies of targeted hypothermia were promising (Bernard et al., 2002; Hypothermia after Cardiac Arrest Study, 2002; Marion et al., 1997), larger multi-center clinical trials failed to confirm these initial observations (Andrews et al., 2015; Nielsen et al., 2013). One potential reason for this discrepancy between mice and humans might be the underlying mechanisms that control the hypothermic response. During targeted hypothermia, the periphery is cooled to lower the core temperature, leaving the brain to defend a higher temperature set point, which causes an increase in metabolic rate. Indeed, one of the common side effects for targeted hypothermia is uncontrolled shivering (Polderman, 2004). In contrast, hypothermia in mice (as reported here) or during daily torpor in heterotherms is achieved by lowering of metabolic rate, which promotes tissue and disease tolerance. Together with observations in torpid and hibernating mammals (Quinones et al., 2014), our findings suggest that energy conserving hypometabolic states, which promote dormancy, might have evolved as a mechanism for tissue tolerance.

Limitations and Open Questions

One limitation of this study is that we investigated the mechanisms of trade-offs and their impact on host defense strategies using a model with two variables: immunity and homeothermy. However, it remains plausible that this simple model might not be sufficient to explain the trade-offs or resource prioritization that occurs in the natural environment when multiple maintenance programs concurrently compete for limited resources. This study also raises many additional questions. First, what signals are released by immune cells to trigger the trade-off that results in energy conservation. Second, how and where are competing demands for energy sensed and prioritized in the brain. Third, how do hypometabolic states enhance tissue tolerance.

STAR Methods

CONTACT FOR REAGENT AND RESOURCE SHARING

Further information and requests for resources and reagents should be directed to and will be fulfilled by the Lead Contact, Ajay Chawla (ajay.chawla@ucsf.edu).

EXPERIMENTAL MODEL AND SUBJECT DETAILS

Mice—Animal studies were conducted under an approved Institutional Animal Care and Use Committee (IACUC) protocol at University of California, San Francisco (UCSF). Mice were congenic to the C57BL6/J background, and housed at 22°C or 30°C (as indicated in the text) under a 12-hr light:dark cycle. Majority of the studies were performed with 10–12-week-old female mice with male mice used where indicated. Mice were adapted at 30°C in laboratory incubator (Darwin Chambers) for 1–3 weeks prior to initiation of studies at thermoneutrality. C57BL/6J (Stock No: 000664), *Tlr4*$^{-/-}$ (Stock No: 029015), *MyD88*$^{-/-}$

(Stock No: 009088), *Tlr4*$^{f/f}$ (Stock No: 024872), *Myd88*$^{f/f}$ (Stock No: 008888), *Lyz2*^{Cre} (Stock No: 004781), and *Vav1*^{Cre} (Stock No: 008610) were purchased from Jackson Laboratories and bred to generate the appropriate alleles. *Ucp1*$^{-/-}$ (*Ucp1*^{tm1Kz}) and *Angptl4*$^{-/-}$ (*Angptl4*^{tm1Jig}) mice were kindly provided by Dr. Kirichok (UCSF) and Dr. Koliwad (UCSF), respectively. For every other day fasting (EODF) studies, mice were adapted to 30°C for 3–4 days prior to initiation of EODF. Both *ad libitum* fed and EODF mice were moved to a clean cage without food at 3pm (ZT 15) for 24 hours followed by addition of food to the EODF mouse cages for 24 hours on the subsequent day. We used this protocol of EODF to minimize the effects of coprophagia on caloric intake. For survival studies with *Ucp1*$^{-/-}$ mice, C57BL/6J and *Ucp1*$^{-/-}$ mice were injected with 1 mg/kg of LPS and temperature was monitored. Mice were euthanized when their core temperature was ≤ 28°C or when they were found unresponsive in cage (absolute survival). To assess absolute survival in C57BL/6J mice, female mice housed at 22°C or 30°C were injected with 3 mg/kg LPS via intra-peritoneal route and monitored every 4–5 hours. Mice were identified as being dead when they were found to be unresponsive in the cage. For body composition analysis, mice were anesthetized with isoflurane prior to DEXA. Experiments were repeated 2–3 independent times.

METHOD DETAILS

Energy expenditure studies with TLR ligands in mice—CLAMS chambers (Columbus Instruments) housed in a temperature controlled environmental chamber were used to quantify energy expenditure. Oxygen consumption rate (VO_2), CO_2 release rate (VCO_2), food intake, and activity were recorded after 1–2-day acclimation in the CLAMS chamber. Conscious mice were administered TLR ligands at indicated doses. Pam3CSK4 (1 and 10 mg/kg, i.p.), Flagellin from *S. typhimurium* (0.5 mg/kg, i.p.), Imiquimod R837 (10 mg/kg, i.p.), ODN1826 (2.5 mg/kg, i.p.), ODN1585 (5 mg/kg, i.p.), Poly (I:C) LMW (40 mg/kg, i.p.) and HKLM (2.5×10^9 per mouse, i.p.) were purchased from Invivogen. PGN from *Bacillus subtilis* (69554) (2.5, 5, and 10 mg/kg, i.p.) was purchased from Sigma Aldrich. LPS (from *E. coli* serotype O111:B4, catalogue # L3024–25 mg) was purchased from Sigma Aldrich, reconstituted in sterile saline at 5 mg/ml, and stored in 100 μl aliquots at −20°C. During the course of our experiments, we used 5 different lots of LPS and observed small variations in the potency of LPS amongst these 5 lots. Thus, to standardize each lot, a dose response curve for suppression of VO_2 was performed in C57BL6/J female mice housed at 22°C. Dose of LPS that significantly suppressed metabolic rate (ranging from 1–1.5 mg/kg) was selected for the subsequent experiments.

Temperature measurements in mice—For measurement of core temperature by telemetry, E-mitters (Starr Life Sciences Corp.) were implanted into the abdominal cavity of mice under anesthesia. After surgery, mice were singly housed and allowed to recover for 10 days. For experiments, cages were placed on a receiving platform (ER-4000 Receiver, Starr Life Sciences Corp.), and temperature and activity data were acquired via Vital View every 10 minutes. To induce hypothermia in mice after surgery, LPS was administered at a dose of 2.25 mg/kg. In a subset of experiments, rectal temperature was also measured using the BAT-12 microprobe thermometer with RET-3 thermocouple (PhysiTemp). Infrared thermography was performed using FLIR E60 to monitor dorsal body temperature non-

invasively at various time points after injection of LPS. Images were taken from 40 cm distance perpendicular to the dorsal surface of the mouse and analyzed using FLIR Tools for Mac.

Infection studies in mice—For *E. coli* infections, *Escherichia coli* (strain O111:B4) was obtained from the laboratory of Dr. Judith Hellman (UCSF). *E. coli* was grown to log phase in LB Broth (Sigma), washed once in PBS, and resuspended in fresh LB Broth. Mice were retro-orbitally injected with 1×10^7 colony-forming units (CFU) diluted in saline for analysis of bacterial burden. For survival experiments, mice were injected with 1×10^8 CFU. Body mass and core temperature were monitored daily.

Listeria monocytogenes (10403S) was obtained from laboratory of Dr. Ari Molofsky (UCSF). *L. monocytogenes* was grown to log phase in BHI Broth (Oxoid). Mice were retro-orbitally injected with 1×10^4 CFU. Pathogen load was determined in spleen and liver for *E. coli* (day 1) and in liver for *L. monocytogenes* (day 4) infections. Spleen and liver were homogenized under sterile conditions in PBS. Serial dilutions for tissues were plated on LB Agar (*E. coli*) or BHI Agar (*L. monocytogenes*) and incubated for 24 hours at 37°C. Plasma was co llected for cytokine and metabolite analysis at indicated times post-infection.

Blood and plasma analyses in mice—Blood glucose measurements were made using glucometer (Bayer). β-hydroxybutrate, creatinine, and triglycerides (plasma and liver) were quantified using commercially available kits as per manufacturer's protocols (Cayman Chemicals). Concentrations of plasma cytokines (IL-6, TNF, IL-10, MCP1, IL12p70, IFNγ) were determined using Mouse Inflammation CBA kit (BD Biosciences). Blood urea nitrogen (BioAssay Systems), troponin (LifeSpan Biosciences), Serum Amyloid A (abcam), Creatine Kinase (abcam), and Angptl4 (abcam) were quantified in plasma using kits and instructions from the respective companies. All plasma samples were stored at −80°C prior to analysis.

Flow cytometry—Peritoneal cavity of mice was flushed with 8 ml of PBS. Cells were pelleted, washed, and re-suspended in FACS buffer (PBS, 5 mM EDTA, 2.5% FBS) for immunostaining and flow cytometric analyses. Titrated amounts of the following antibodies from BioLegend were used: CD45 (clone 30-F11), CD11b (clone M1/70), F4/80 (clone BM8), CD19 (clone 6D5), CD5 (clone 53–7.3) and TLR4 (clone SA15–21). Data were acquired using FACSVerse (BD) and analyzed using FlowJo software.

Respiratory supercomplex activity—For analysis of RSCs, mitochondria were isolated from tissues (liver, heart, and BAT) at various time points after administration of LPS to mice housed at 22°C or 30°C. BN-PAGE analyses were performed as described by Jha et. al. (Jha et al., 2016). Purified mitochondria were suspended in solubilization buffer (50 mM Imidazole, 500 mM 6-aminocaproic acid, 1 mM EDTA, pH 7.0) at a concentration of 5 mg protein/ml with digitonin (ratio of 2 g/g of digitonin/protein). After 30-min incubation on ice, samples were centrifuged at 20,000g for 30 min to obtain solubilized proteins. Coomassie brilliant blue G-250 (Digitonin/Dye ratio of 4:1) and glycerol (a final concentration of 5%) were added to the samples prior to loading on NativePAGE™ 3–12% Bis-Tris Protein Gels (ThermoFisher Scientific). Electrophoresis was performed at 150 V for 30 min and then the gel was run at 250V for 120 min on ice using the following buffers:

cathode buffer (50 mM tricine, 7.5 mM imidazole and 0.002% Coomassie brilliant blue G-250) and anode buffer (20mM imidazole, pH 7.0). The cathode buffer was changed to a buffer containing 50 mM tricine and 7.5 mM imidazole after the running front had migrated about one-third of the total running distance from the bottom of the gel. In-gel activity assays were used to detect complexes containing complex I, II and IV, and SDS–PAGE with immunoblotting was used to detect complex III (UQCRC2, Clone 13G12AF12BB11, abcam #ab14745) and complex V (ATP5A, Clone 15H4C4, abcam #ab14748).

For in gel assays, gels were incubated with complex I substrate solution (2 mM Tris-HCl, pH 7.4, 0.1 mg/mL NADH, and 2.5 mg/mL nitrotetrazolium blue chloride), complex II substrate solution (5 mM Tris-HCl, pH 7.4, 0.2 mM phenazine methosulfate, 2.5 mg/mL nitrotetrazolium blue chloride, and 20 mM sodium succinate), or complex IV substrate solution (25 mM KPO4, pH 7.2, 20 uM reduced cytochrome c, and 0.5 mg/mL diaminobenzidine) at room temperature. After the bands appeared, the reaction was stopped with 10% acetic acid. The gels were subsequently washed with water and scanned. Representative results are shown in figures.

For immunoblotting, snap-frozen brown fat was homogenized in buffer containing 50 mM Tris pH 7.5, 150 mM NaCl, 0.1 % (w/v) SDS, 0.5 % (w/v) Na-Deoxycholate, 1 % (v/v) NP-40, 1 mM EDTA, 1mM EGTA, and protease inhibitor cocktail (Sigma-Aldrich; #P8340). To test for expressions of target proteins, membranes were first blocked with 5 % milk in 0.1 % TBST and incubated overnight at +4°C with UCP1 (abcam; #10983; 1:1000 dilution in 0.1 % TBST containing 3 % BSA), Ubiquitin (Cell Signaling; #3933S; 1:1000 in 0.1 % TBST containing 3 % BSA), and HSP90 (Cell Signaling; #4874S; 1:1000 dilution in 0.1 % TBST containing 3 % BSA) primary antibodies followed by 1h incubation at room temperature with HRP-conjugated secondary antibody (Cell Signaling; #7074S; 1:10 000 dilution in 0.1 % TBST containing 5 % milk). Immunoblotted proteins were detected using ProSignal Pico Chemiluminescent Substrate. For the ubiquitin blots, lysates were prepared in the presence of proteasomal inhibitor MG132 (Sigma-Aldrich; # M8699) added to final concentration of 1 μM.

Oxygen consumption in tissues—A Clark-type oxygen electrode (Model 782/MT200, Strathkelvin Instruments, Scotland) was used to quantify tissue oxygen consumption. Minced brown adipose, liver, or heart tissue from euthermic and torpid mice was incubated in 500 μl of respiration buffer (4.5 g/L glucose, 2% BSA, 1 mM pyruvate in PBS), and oxygen consumption was quantified. Oxygen consumption rate was calculated using Strathkelvin 782 Oxygen System software (version 4.1).

Metabolomics—Plasma was snap frozen at 0, 4, 12, and 24 hours post-LPS injection. Samples were sent to the UC Davis Metabolomics Core for GC-TOF mass spectrometry analysis of primary metabolites, and LC-TOF mass spectrometry analysis of complex lipids. For quantification of acylcarnitines in plasma and liver, samples were collected 12 hours after injection of mice with LPS, snap frozen, and sent to University of Utah's Metabolomics Core Research Facility for analysis. Detailed methods for sample extraction, LC-MS analysis, and data analysis for the acylcarnitines are provided in Table S1.

RNA-sequencing—We adapted Cel-Seq2 protocol to sequence RNA transcripts in livers of mice treated with LPS. As previously described (Hashimshony et al., 2016), Cel-Seq2 was performed using reverse-transcription primers that contained anchored polyT, a 6 base pair unique barcode, a 6-base pair UMI (unique molecular identifier), the 5' Illumina adaptor as used in the Illumina small RNA kit, and a T7 promoter. Instead of single cells, total RNA isolated from liver was used for linear mRNA amplification. Cel-Seq2 primers (5 ng each) mixed with ERCC RNA spike-in (1:1,000,000 dilution) and water were directly added to 200 ng of purified mRNA, and incubated at 65°C for 5 minutes sample spun down mid-incubation. After the second-strand synthesis, samples were pooled, cleaned using AMPure XP beads, and washed with 80% ethanol before proceeding to the IVT reaction (Ambion kit) for 13 hr. After primer removal, RNA was fragmented in fragmentation buffer (200 mM Tris-acetate pH 8.1, 500 mM KOAc, 150 mM MgOAc) for 95 seconds at 94°C, and the reaction with the addition of one-tenth volume of 0.5 M EDTA on ice. After RNA cleanup with RNAClean XP beads, RNA quality and yield were assayed using a Bioanalyzer (Agilent). A total of 10 ng of RNA was used for library preparation, and the aRNA was converted to cDNA with 3' RNA adaptors sequences (RPI) found in the TruSeq Small RNA Library Prep Pooling Guide. A total of 11 cycles of PCR were performed with an elongation time of 30 seconds. Following cDNA cleanup and dilution, samples were multiplexed and sequenced on Illumina Nextseq 500 using Mid Output v2 Kit.

Quantitative RT-PCR—Purified RNA was reverse transcribed using qScript cDNA SuperMix (Quanta), and quantitative PCR was performed on the cDNA templates using CFX384 real-time PCR detection system (Bio-Rad). Relative mRNA expression level was determined using the 2(-Delta Delta C(T)) method with 36B4 as the internal reference control.

QUANTIFICATION AND STATISTICAL ANALYSIS

Statistical Analysis—Statistical analyses were performed using Prism 7 (GraphPad Software, San Diego, CA USA). Data are presented as mean ± s.e.m. Statistical significance was determined using the unpaired two-tailed Student's t-test (unpaired, 2-tailed) for single variables and two-way ANOVA followed by Bonferroni post-tests for multiple variables. A p-value of < 0.05 was considered to be statistically significant and is presented as * ($p < 0.05$), ** ($p < 0.01$), *** ($p < 0.001$), or **** ($p < 0.0001$). P values for survival curves were calculated using Mantel-Cox or Gehan-Breslow-Wilcoxon test. Biological replicates used in each of the studies are indicated in the figure legends as "n=".

RNA-seq analysis—The RNA-seq reads were clipped to remove PolyA sequences (clipped after 7 bp or longer stretches of A nucleotides) and trimmed with Trimmomatic (parameters: LEADING:15 TRAILING:15 MINLEN:35) (Bolger et al., 2014). Mapping was done using Kallisto with 100 bootstraps (Bray et al., 2016). Differential gene expression analysis was performed using Sleuth in gene-level mode with likelihood-ratio test as the method for statistical testing (Pimentel et al., 2017), and pathway analysis was performed using Metascape (Tripathi et al., 2015).

Metabolomics data processing—Data analysis for polar and non-polar metabolites were performed by UC Davis Metabolomics Core. Briefly, differences in metabolite abundances were determined via two-way ANOVA followed by t test with a Benjamini-Hochberg procedure to identify pairwise changes (Wanichthanarak et al., 2017). Heatmap with hierarchical clustering analysis (distance metric: Euclidian, agglomeration method: complete) was performed on the average intensity of each group level to examine the correlation amongst the metabolites (Wanichthanarak et al., 2017).

Data analysis for acylcarnitines was performed by University of Utah Metabolomics Core Research Facility. Briefly, results from LC-MS experiments are collected using Agilent Mass Hunter Workstation and analyzed using the software package Agilent MassHunter Quant B.07.00. Carnitines were quantitated based on peak area ratios to the isotopically labeled standards added to the extracts.

Supplementary Material

Refer to Web version on PubMed Central for supplementary material.

Acknowledgments

We thank members of the Chawla laboratory and A. Loh for comments on the manuscript, and X. Cui for assistance with mouse husbandry. The authors' work was supported by grants from NIH (DK094641, DK101064). K.G., J.N., K.M., and Y.A.L. were supported by Postdoctoral Fellowships from the T32 training grant (4 T32 HL 7731-25), EMBO (ALTF 1185-2017), and NHMRC (GNT1121917 to K.M. and GNT1142229 to Y.A.L.). Mass spectrometry equipment was obtained through NIH Shared Instrumentation Grant 1S10OD018210-01A1 (J.E.C) and 1S10OD021505-01 (J.E.C).

References

Abram CL, Roberge GL, Hu Y, and Lowell CA (2014). Comparative analysis of the efficiency and specificity of myeloid-Cre deleting strains using ROSA-EYFP reporter mice. J Immunol Methods 408, 89–100. [PubMed: 24857755]

Andrews PJ, Sinclair HL, Rodriguez A, Harris BA, Battison CG, Rhodes JK, Murray GD, and Eurotherm Trial C (2015). Hypothermia for Intracranial Hypertension after Traumatic Brain Injury. The New England journal of medicine 373, 2403–2412. [PubMed: 26444221]

Ayres JS, and Schneider DS (2008). A signaling protease required for melanization in Drosophila affects resistance and tolerance of infections. PLoS Biol 6, 2764–2773. [PubMed: 19071960]

Ayres JS, and Schneider DS (2012). Tolerance of infections. Annual review of immunology 30, 271–294.

Bartelt A, Bruns OT, Reimer R, Hohenberg H, Ittrich H, Peldschus K, Kaul MG, Tromsdorf UI, Weller H, Waurisch C, et al. (2011). Brown adipose tissue activity controls triglyceride clearance. Nat Med 17, 200–205. [PubMed: 21258337]

Bernard SA, Gray TW, Buist MD, Jones BM, Silvester W, Gutteridge G, and Smith K (2002). Treatment of comatose survivors of out-of-hospital cardiac arrest with induced hypothermia. The New England journal of medicine 346, 557–563. [PubMed: 11856794]

Bodine SC, Latres E, Baumhueter S, Lai VK, Nunez L, Clarke BA, Poueymirou WT, Panaro FJ, Na E, Dharmarajan K, et al. (2001). Identification of ubiquitin ligases required for skeletal muscle atrophy. Science 294, 1704–1708. [PubMed: 11679633]

Bolger AM, Lohse M, and Usadel B (2014). Trimmomatic: a flexible trimmer for Illumina sequence data. Bioinformatics 30, 2114–2120. [PubMed: 24695404]

Bray NL, Pimentel H, Melsted P, and Pachter L (2016). Near-optimal probabilistic RNA-seq quantification. Nat Biotechnol 34, 525–527. [PubMed: 27043002]

Cannon B, and Nedergaard J (2011). Nonshivering thermogenesis and its adequate measurement in metabolic studies. The Journal of experimental biology 214, 242–253. [PubMed: 21177944]

De Benedetti F, Alonzi T, Moretta A, Lazzaro D, Costa P, Poli V, Martini A, Ciliberto G, and Fattori E (1997). Interleukin 6 causes growth impairment in transgenic mice through a decrease in insulin-like growth factor-I. A model for stunted growth in children with chronic inflammation. J Clin Invest 99, 643–650. [PubMed: 9045866]

DiAngelo JR, Bland ML, Bambina S, Cherry S, and Birnbaum MJ (2009). The immune response attenuates growth and nutrient storage in Drosophila by reducing insulin signaling. Proc Natl Acad Sci U S A 106, 20853–20858. [PubMed: 19861550]

Dibner JJ, and Richards JD (2005). Antibiotic growth promoters in agriculture: history and mode of action. Poult Sci 84, 634–643. [PubMed: 15844822]

Dijk W, Heine M, Vergnes L, Boon MR, Schaart G, Hesselink MK, Reue K, van Marken Lichtenbelt WD, Olivecrona G, Rensen PC, et al. (2015). ANGPTL4 mediates shuttling of lipid fuel to brown adipose tissue during sustained cold exposure. Elife 4.

Ganeshan K, and Chawla A (2014). Metabolic regulation of immune responses. Annual review of immunology 32, 609–634.

Ganeshan K, and Chawla A (2017). Warming the mouse to model human diseases. Nature reviews Endocrinology 13, 458–465.

Garaude J, Acin-Perez R, Martinez-Cano S, Enamorado M, Ugolini M, Nistal-Villan E, Hervas-Stubbs S, Pelegrin P, Sander LE, Enriquez JA, et al. (2016). Mitochondrial respiratory-chain adaptations in macrophages contribute to antibacterial host defense. Nat Immunol 17, 1037–1045. [PubMed: 27348412]

Geiser F (2004). Metabolic rate and body temperature reduction during hibernation and daily torpor. Annu Rev Physiol 66, 239–274. [PubMed: 14977403]

Hagar JA, Powell DA, Aachoui Y, Ernst RK, and Miao EA (2013). Cytoplasmic LPS activates caspase-11: implications in TLR4-independent endotoxic shock. Science 341, 1250–1253. [PubMed: 24031018]

Harms M, and Seale P (2013). Brown and beige fat: development, function and therapeutic potential. Nat Med 19, 1252–1263. [PubMed: 24100998]

Hashimshony T, Senderovich N, Avital G, Klochendler A, de Leeuw Y, Anavy L, Gennert D, Li S, Livak KJ, Rozenblatt-Rosen O, et al. (2016). CEL-Seq2: sensitive highly-multiplexed single-cell RNA-Seq. Genome Biol 17, 77. [PubMed: 27121950]

Hypothermia after Cardiac Arrest Study, G. (2002). Mild therapeutic hypothermia to improve the neurologic outcome after cardiac arrest. The New England journal of medicine 346, 549–556. [PubMed: 11856793]

Jamieson AM, Pasman L, Yu S, Gamradt P, Homer RJ, Decker T, and Medzhitov R (2013). Role of tissue protection in lethal respiratory viral-bacterial coinfection. Science 340, 1230–1234. [PubMed: 23618765]

Jha P, Wang X, and Auwerx J (2016). Analysis of Mitochondrial Respiratory Chain Supercomplexes Using Blue Native Polyacrylamide Gel Electrophoresis (BN-PAGE). Curr Protoc Mouse Biol 6, 1–14. [PubMed: 26928661]

Kayagaki N, Wong MT, Stowe IB, Ramani SR, Gonzalez LC, Akashi-Takamura S, Miyake K, Zhang J, Lee WP, Muszynski A, et al. (2013). Noncanonical inflammasome activation by intracellular LPS independent of TLR4. Science 341, 1246–1249. [PubMed: 23887873]

Knottnerus SJG, Bleeker JC, Wust RCI, Ferdinandusse S, L IJ, Wijburg FA, Wanders RJA, Visser G, and Houtkooper RH (2018). Disorders of mitochondrial long-chain fatty acid oxidation and the carnitine shuttle. Rev Endocr Metab Disord

Lochmiller RL, and Deerenberg C (2000). Trade-offs in evolutionary immunology: just what is the cost of immunity? Oikos 88, 87–98.

Marion DW, Penrod LE, Kelsey SF, Obrist WD, Kochanek PM, Palmer AM, Wisniewski SR, and DeKosky ST (1997). Treatment of traumatic brain injury with moderate hypothermia. The New England journal of medicine 336, 540–546. [PubMed: 9023090]

McDade TW (2005). Life history, maintenance, and the early origins of immune function. Am J Hum Biol 17, 81–94. [PubMed: 15612049]

Medzhitov R, Schneider DS, and Soares MP (2012). Disease tolerance as a defense strategy. Science 335, 936–941. [PubMed: 22363001]

Melvin RG, and Andrews MT (2009). Torpor induction in mammals: recent discoveries fueling new ideas. Trends Endocrinol Metab 20, 490–498. [PubMed: 19864159]

Nielsen N, Wetterslev J, Cronberg T, Erlinge D, Gasche Y, Hassager C, Horn J, Hovdenes J, Kjaergaard J, Kuiper M, et al. (2013). Targeted temperature management at 33 degrees C versus 36 degrees C after cardiac arrest. The New England journal of medicine 369, 2197–2206. [PubMed: 24237006]

Noda C, and Ichihara A (1976). Control of ketogenesis from amino acids. IV. Tissue specificity in oxidation of leucine, tyrosine, and lysine. J Biochem 80, 1159–1164. [PubMed: 1002682]

O'Neill LA, and Pearce EJ (2016). Immunometabolism governs dendritic cell and macrophage function. The Journal of experimental medicine 213, 15–23. [PubMed: 26694970]

Odegaard JI, and Chawla A (2013). Pleiotropic actions of insulin resistance and inflammation in metabolic homeostasis. Science 339, 172–177. [PubMed: 23307735]

Pimentel H, Bray NL, Puente S, Melsted P, and Pachter L (2017). Differential analysis of RNA-seq incorporating quantification uncertainty. Nature methods 14, 687–690. [PubMed: 28581496]

Polderman KH (2004). Application of therapeutic hypothermia in the intensive care unit. Opportunities and pitfalls of a promising treatment modality--Part 2: Practical aspects and side effects. Intensive Care Med 30, 757–769. [PubMed: 14767590]

Quinones QJ, Ma Q, Zhang Z, Barnes BM, and Podgoreanu MV (2014). Organ protective mechanisms common to extremes of physiology: a window through hibernation biology. Integr Comp Biol 54, 497–515. [PubMed: 24848803]

Raberg L, Graham AL, and Read AF (2009). Decomposing health: tolerance and resistance to parasites in animals. Philos Trans R Soc Lond B Biol Sci 364, 37–49. [PubMed: 18926971]

Raberg L, Sim D, and Read AF (2007). Disentangling genetic variation for resistance and tolerance to infectious diseases in animals. Science 318, 812–814. [PubMed: 17975068]

Rakhshandehroo M, Knoch B, Muller M, and Kersten S (2010). Peroxisome proliferator-activated receptor alpha target genes. PPAR Res 2010.

Rauw WM (2012). Immune response from a resource allocation perspective. Front Genet 3, 267. [PubMed: 23413205]

Reeds PJ, and Jahoor F (2001). The amino acid requirements of disease. Clin Nutr 20, 15–22.

Sadd BM, and Schmid-Hempel P (2009). Principles of ecological immunology. Evol Appl 2, 113–121. [PubMed: 25567851]

Schieber AM, Lee YM, Chang MW, Leblanc M, Collins B, Downes M, Evans RM, and Ayres JS (2015). Disease tolerance mediated by microbiome E. coli involves inflammasome and IGF-1 signaling. Science 350, 558–563. [PubMed: 26516283]

Simcox J, Geoghegan G, Maschek JA, Bensard CL, Pasquali M, Miao R, Lee S, Jiang L, Huck I, Kershaw EE, et al. (2017). Global Analysis of Plasma Lipids Identifies Liver-Derived Acylcarnitines as a Fuel Source for Brown Fat Thermogenesis. Cell Metab 26, 509–522 e506. [PubMed: 28877455]

Simms EL, and Triplett J (1994). Costs and Benefits of Plant-Responses to Disease - Resistance and Tolerance. Evolution 48, 1973–1985. [PubMed: 28565152]

Soares MP, Teixeira L, and Moita LF (2017). Disease tolerance and immunity in host protection against infection. Nat Rev Immunol 17, 83–96. [PubMed: 28044057]

Stearns SC (1992). The evolution of life histories (Oxford ; New York: Oxford University Press).

Tan Y, and Kagan JC (2014). A cross-disciplinary perspective on the innate immune responses to bacterial lipopolysaccharide. Molecular cell 54, 212–223. [PubMed: 24766885]

Thompson CB (2011). Rethinking the regulation of cellular metabolism. Cold Spring Harb Symp Quant Biol 76, 23–29. [PubMed: 22429931]

Torres BY, Oliveira JH, Thomas Tate A, Rath P, Cumnock K, and Schneider DS (2016). Tracking Resilience to Infections by Mapping Disease Space. PLoS Biol 14, e1002436. [PubMed: 27088359]

Tripathi S, Pohl MO, Zhou Y, Rodriguez-Frandsen A, Wang G, Stein DA, Moulton HM, DeJesus P, Che J, Mulder LC, et al. (2015). Meta- and Orthogonal Integration of Influenza "OMICs" Data Defines a Role for UBR4 in Virus Budding. Cell Host Microbe 18, 723–735. [PubMed: 26651948]

Tucker VA (1962). Diurnal torpidity in the California pocket mouse. Science 136, 380–381. [PubMed: 13923001]

Wang A, Huen SC, Luan HH, Yu S, Zhang C, Gallezot JD, Booth CJ, and Medzhitov R (2016). Opposing Effects of Fasting Metabolism on Tissue Tolerance in Bacterial and Viral Inflammation. Cell 166, 1512–1525 e1512. [PubMed: 27610573]

Wanichthanarak K, Fan S, Grapov D, Barupal DK, and Fiehn O (2017). Metabox: A Toolbox for Metabolomic Data Analysis, Interpretation and Integrative Exploration. PLoS One 12, e0171046. [PubMed: 28141874]

Weis S, Carlos AR, Moita MR, Singh S, Blankenhaus B, Cardoso S, Larsen R, Rebelo S, Schauble S, Del Barrio L, et al. (2017). Metabolic Adaptation Establishes Disease Tolerance to Sepsis. Cell 169, 1263–1275 e1214. [PubMed: 28622511]

Zuk M, and Stoehr AM (2002). Immune defense and host life history. Am Nat 160 Suppl 4, S9–S22. [PubMed: 18707455]

Highlights

1. Activated immunity engages in an energetic trade-off with homeothermy.
2. Immunity reprograms hepatic metabolism to meet host energetic priorities.
3. Energetic trade-off between immunity and homeothermy promotes disease tolerance.
4. Hypometabolic states promote disease tolerance during bacterial infections.

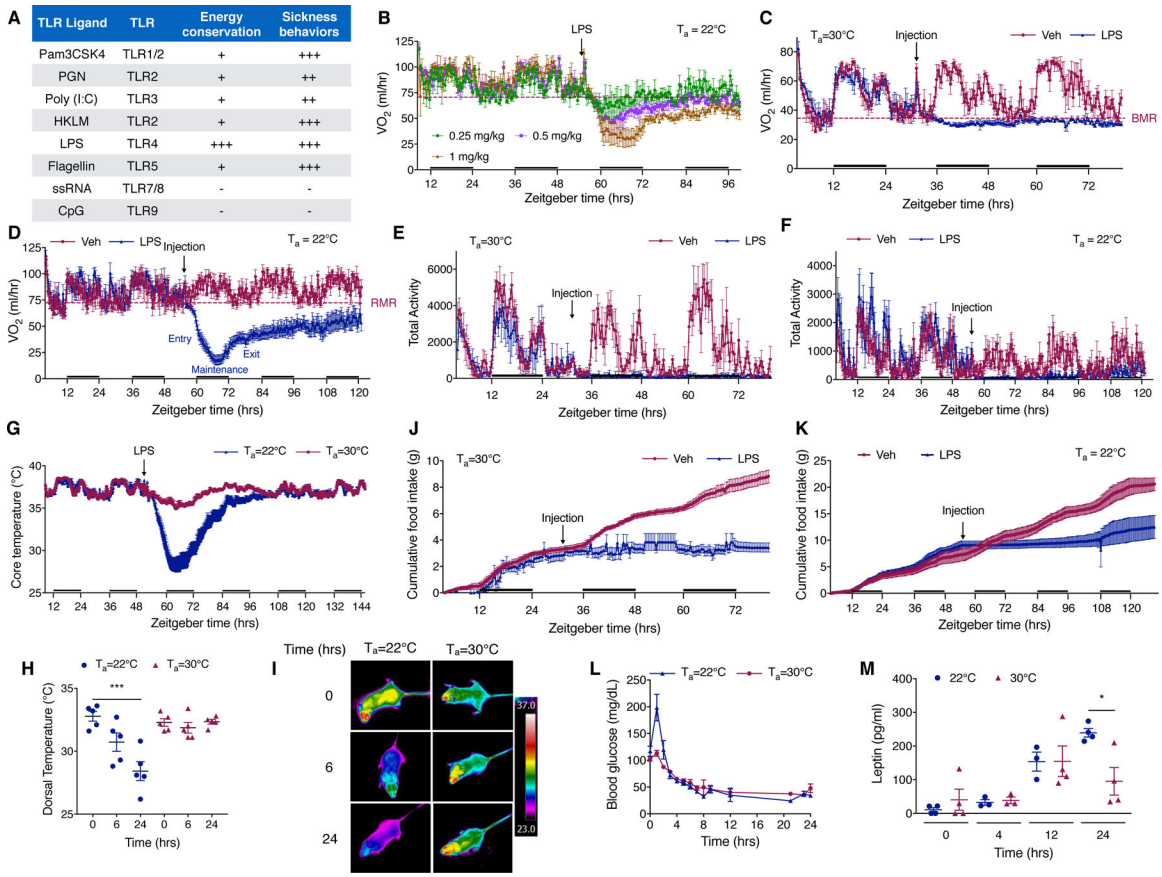

Figure 1. Activation of immunity by LPS promotes energy conservation.

(A) Summary of the effects of TLR ligands on energy conservation and sickness behaviors. (B) Rate of oxygen consumption (VO_2) in mice housed at 22°C and treated with various doses of LPS (n=3 mice per dose). (C, D) Rate of oxygen consumption (VO_2) in mice housed at 22°C (C) or 30°C (D) and treated with vehicle or LPS (n=4–8 mice per treatment and temperature). Three stages (entry, maintenance, and exit) of the hypometabolic state are indicated (D). (E, F) Total activity in mice housed at 30°C (E) or 22°C (F) and treated with vehicle or LPS (n=4–8 mice per treatment and temperature). (G) Core temperature of mice housed at 22°C or 30°C that were treated with vehicle or LPS (n=6 mice per treatment and temperature). (H, I) Infrared measurements of dorsal surface temperature of mice housed at 30°C or 22°C that were treated with vehicle or LPS (n=5 mice per treatment and temperature); dorsal surface temperature (H) and representative images (I). (J, K) Cumulative food intake in mice housed at 30°C (J) or 22°C (K) that were with vehicle or LPS (n=4–8 mice per treatment and temperature). (L) Blood glucose levels in mice treated with LPS that were housed at 22°C or 30°C (n=12–13 mice per temperature, pooled from multiple experiments). (M) Plasma levels of leptin at various time points after administration of LPS to mice housed at 22°C or 30°C (n=3–4 mice per time point and temperature). Data are presented as mean ± SEM. *p < 0.05, ***p < 0.001. See also Figure S1 and S2.

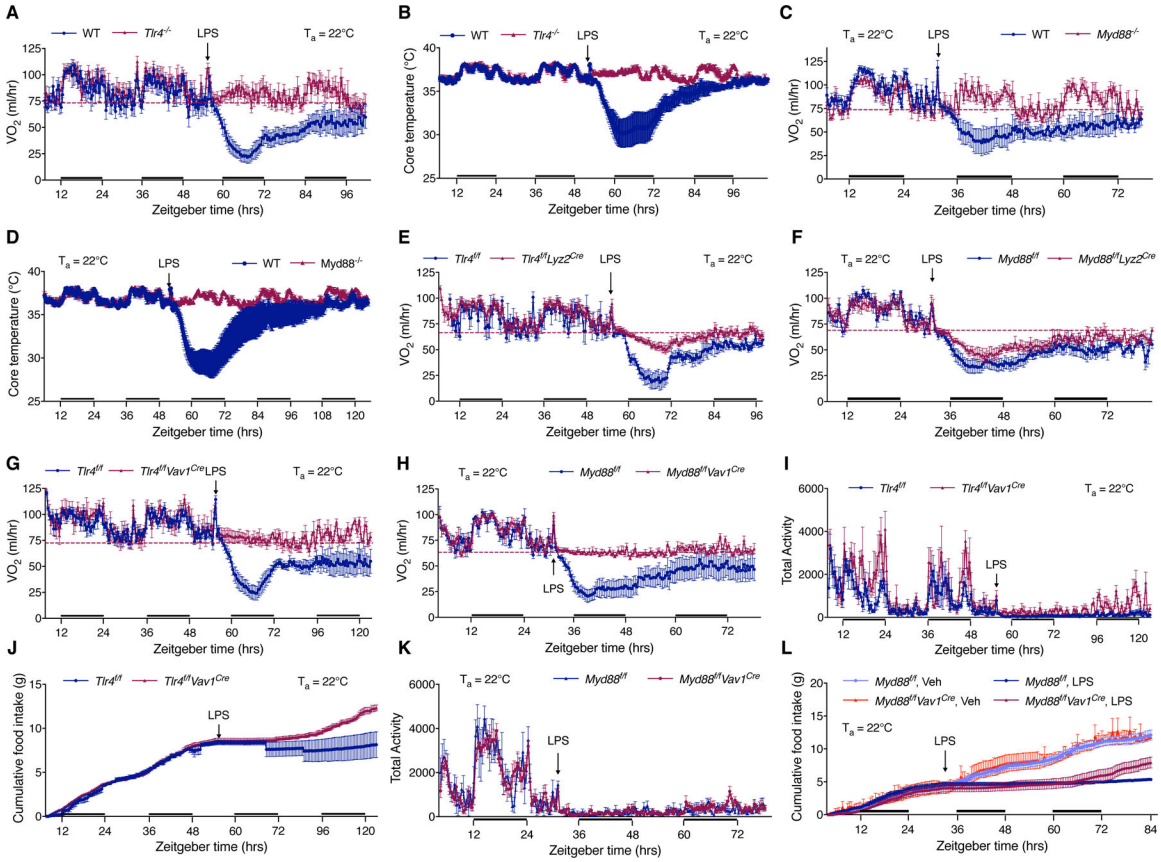

Figure 2. Hematopoietic sensing of LPS via TLR4/MyD88 triggers energy conservation independent of sickness behaviors.

(A) Rate of oxygen consumption (VO_2) in C57BL/6J (n=5) and *Tlr4*$^{-/-}$ (n=6) mice treated with LPS at 22°C. (B) Core temperature of C57BL/6J (n=6) and *Tlr4*$^{-/-}$ (n=5) mice treated with LPS at 22°C. (C) Rate of oxygen consumption (VO_2) in C57BL/6J (n=5) and *Myd88*$^{-/-}$ (n=5) mice treated with LPS at 22°C. (D) Core temperature of C57BL/6J (n=5) and *Myd88*$^{-/-}$ (n=6) mice treated with LPS at 22°C. (E, F) Rate of oxygen consumption (VO_2) in *Tlr4*$^{f/f}$ (n=3) and *Tlr4*$^{f/f}$*Lyz2*^{Cre} (n=9), or *Myd88*$^{f/f}$ (n=6) and *Myd88*$^{f/f}$*Lyz2*^{Cre} (n=7) mice treated with LPS at 22°C (data pooled from multiple experiments). (G, H) Rate of oxygen consumption (VO_2) in *Tlr4*$^{f/f}$ (n=5) and *Tlr4*$^{f/f}$*Vav1*^{Cre} (n= 4) male mice, or *Myd88*$^{f/f}$ (n=4) and *Myd88*$^{f/f}$*Vav1*^{Cre} (n=8) female mice treated with LPS at 22°C (data pooled from multiple experiments). (I, J) Total activity (I) and cumulative food intake (J) in *Tlr4*$^{f/f}$ (n=5) and *Tlr4*$^{f/f}$*Vav1*^{Cre} (n=4) male mice treated with LPS at 22°C (data pooled from multiple experiments). (K, L) Total activity (K) and cumulative food intake (L) in *Myd88*$^{f/f}$ (n=4) and *Myd88*$^{f/f}$*Vav1*^{Cre} (n=8) female mice treated with LPS at 22°C (data pooled from multiple experiments). Data are presented as mean ± SEM. See also Figure S2 and S3.

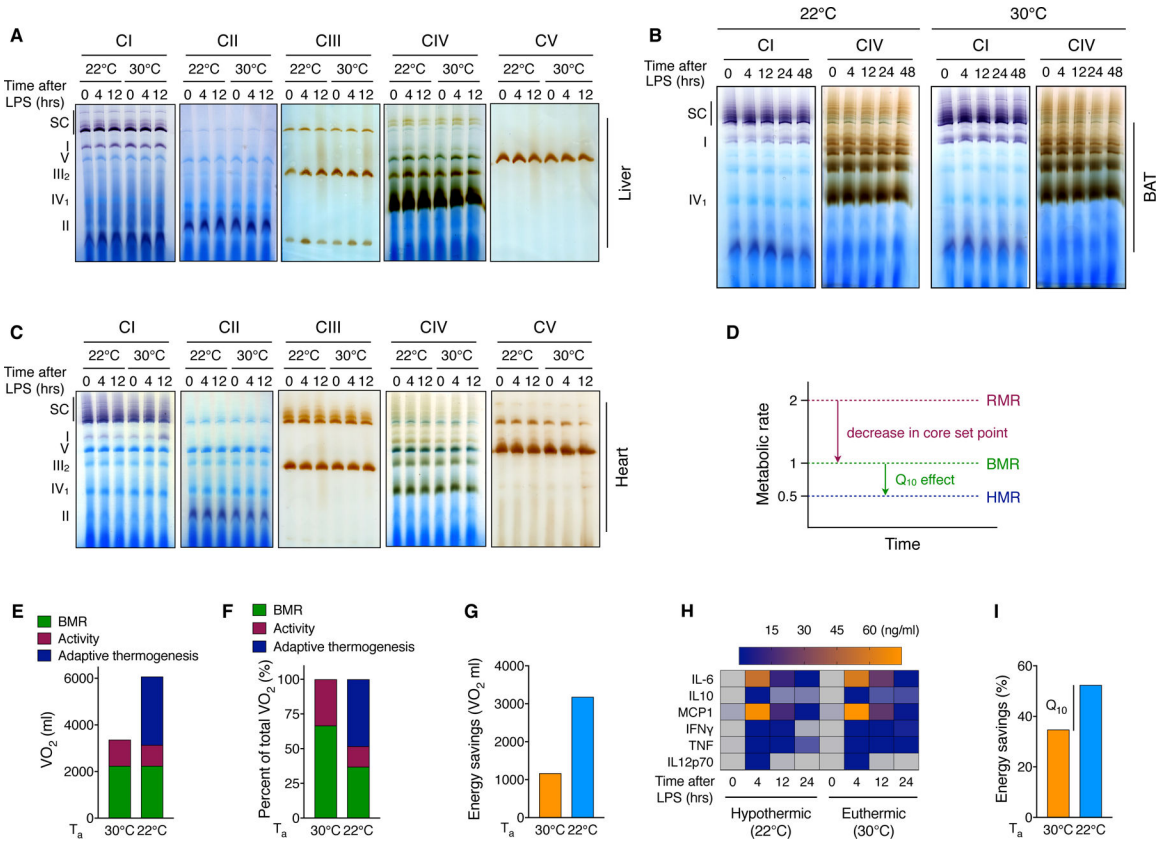

Figure 3. Shift in core set point and Q_{10} effect suppresses metabolic rate to initiate physiologic trade-off with homeothermy.

(A-C) Temporal analysis of RSC assembly and activity in liver, BAT, and heart of mice treated with LPS. BN-PAGE coupled with in-gel activity assays were used to detect CI- and CIV-containing RSCs, and CII. CIII and CV were detected by immunoblotting. (D) Model for suppression of metabolic rate during LPS-induced hypothermia. RMR: resting metabolic rate at 22°C; BMR: basal metabolic rate at 30°C; HMR: hypothermic metabolic rate. (E, F) Quantification of absolute (E) and relative (F) energetic costs of maintenance programs in mice housed at 22°C or 30°C. (G) Quantification of absolute energy savings in mice treated with LPS at 22°C or 30°C. (H) Quantification of plasma cytokines at various times after treatment of mice with LPS housed at 22°C or 30°C (n=5–10 mice per time point and temperature). SEM values are presented as a heat map. (I) Quantification of relative energy savings in mice treated with LPS at 22°C or 30°C. See also Figure S4.

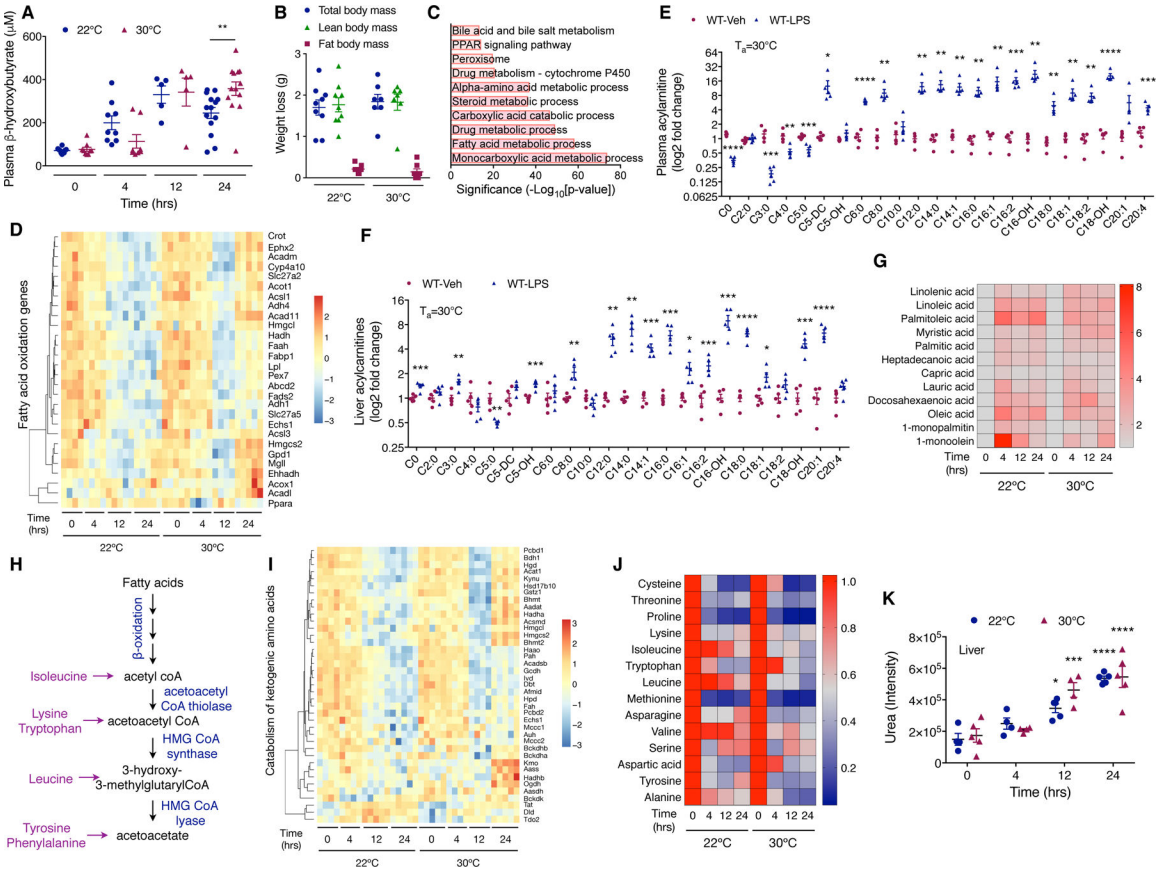

Figure 4. Activation of immunity reprograms nutrient metabolism in the liver.

(A) Quantification of β-hydroxybutyrate in plasma of mice treated with LPS (n= 5–14 mice per time point and temperature, pooled from multiple experiments). (B) Quantification of total body, lean, and fat mass in mice administered LPS (n=7–9 mice per temperature, data compiled from multiple experiments). (C) Pathways or processes (Gene Ontologies and IPA) significantly enriched in downregulated genes at the 12-hour time point. (D) Heat maps of genes involved in fatty acid oxidation in livers of mice treated with LPS at 22°C and 30°C (n=4–5 mice per temperature and treatment). (E, F) LC-MS analysis of acylcarnitines in plasma (E) and liver (F) of mice treated with LPS for 12 hours at 30°C (n=5 mice per treatment). Data plotted as log2 fold change. (G) GC-MS analysis of fatty acids in plasma of mice treated with LPS (n=4–5 mice per temperature and time point). (H) Schematic of biochemical pathways involved in ketogenesis in liver; metabolites (black), enzymes (blue), and amino acids (purple). (I) Heat map of genes involved in catabolism of amino acids in livers of mice treated with LPS at 22°C and 30°C (n=4–5 mice per temperature and treatment). (J) GC-MS analysis of amino acids in plasma of mice treated with LPS (n=4–5 mice per temperature and time point). (K) GC-MS analysis of urea in livers of mice treated with LPS (n=4–5 mice per temperature and time point). Mean values are presented in heat maps for plasma metabolites and gene expression, and other data are presented as mean ± SEM. *p < 0.05; **p < 0.01; ***p < 0.001; ****p < 0.0001. See also Figure S5 and Tables S1–3.

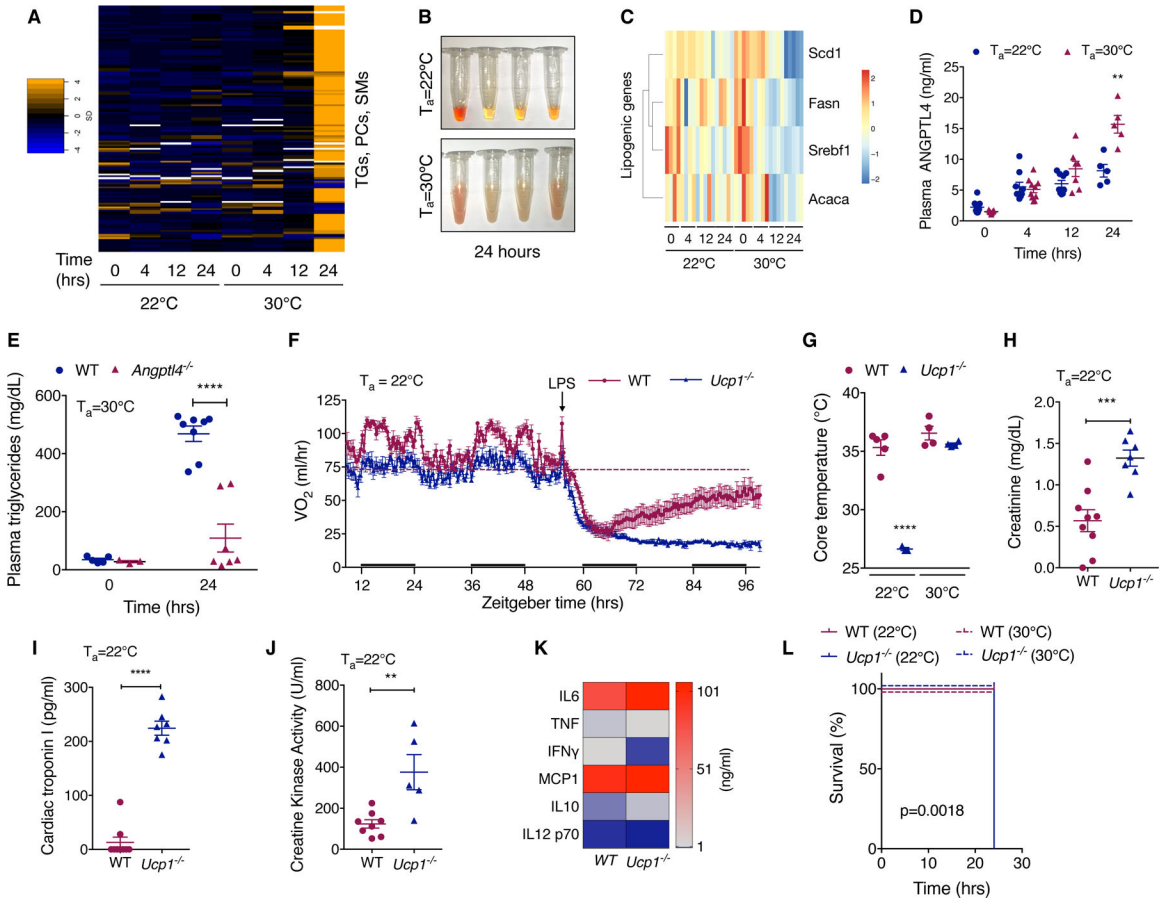

Figure 5. BAT thermogenesis generates heat for exit from hypothermic state.

(A) LC-MS analysis for lipids in plasma of mice treated with LPS (n=4–5 mice per temperature and time point). (B) Photograph of plasma collected at 24 hours after administration of LPS to mice. (C) Heat map of lipogenesis genes in livers of mice treated with LPS (n=4–5 mice per time point and temperature). (D) Quantification of ANGPTL4 by ELISA in plasma of mice treated with LPS (n=5–10 mice per time point and temperature). (E) Quantification of plasma triglycerides 24 hours after administration of LPS to WT and *Angptl4*$^{-/-}$ mice that were housed at 30°C (n=3–8 mice per time point and genotype, pooled from multiple experiments). (F) Core temperature of C57BL/6J and *Ucp1*$^{-/-}$ mice 24 hours after treatment with LPS (n=3–5 mice per genotype and temperature). (G) Rate of oxygen consumption (VO_2) in C57BL/6J (n=10) and *Ucp1*$^{-/-}$ (n=7) mice treated with LPS at 22°C. (H-J) Quantification of tissue damage biomarkers in plasma of C57BL/6J (n=4–9) and *Ucp1*$^{-/-}$ (n=4–7) mice 24 hours after treatment with LPS at 22°C; Creatinine (H), Cardiac troponin I (I), Creatine kinase (J). (K) Quantification of plasma cytokines 4 hours after treatment of C57BL/6J and *Ucp1*$^{-/-}$ mice with LPS at 22°C (n=8–10 mice per time point and temperature). Mean values are presented as a heat map. (L) Kaplan-Meier survival curves of C57BL/6J (n=5) and *Ucp1*$^{-/-}$ (n=5) mice treated with LPS at 22°C and 30°C. Data are presented as mean ± SEM. **p < 0.01, ***p < 0.001, ****p < 0.0001. See also Figure S6.

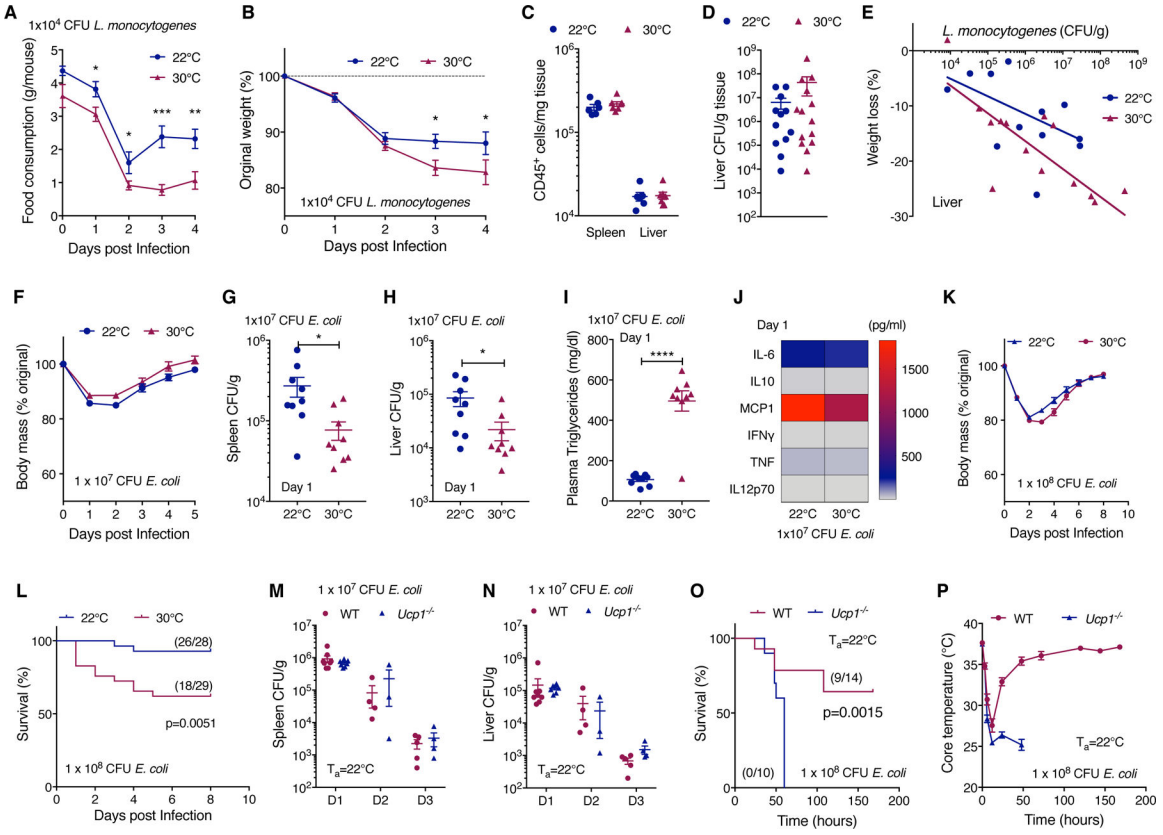

Figure 6. Competition for energy promotes plasticity in host defense strategies.

(A, B) Food consumption (A) and change in body weight (B) after injection of 1×10^4 CFUs of wild type *L. monocytogenes* into mice housed at 22°C and 30°C (n=13–14 mice per temperature; data combined from 2 separate experiments). (C) Flow cytometric quantification of $CD45^+$ cells in liver and spleen 4 days post-infection with *L. monocytogenes* (n=6–7 mice per temperature). (D) Liver CFUs 4-days post-infection with *L. monocytogenes* (1×10^4 CFU, n=12–14 mice per temperature, data pooled from 2 experiments). (E) Reaction norm plots of host health (weight loss) and pathogen burden (*L. monocytogenes* CFU in liver) 4-days post-infection (n=12–14 mice per temperature, data pooled from 2 experiments). (F) Body mass of mice infected with *E. coli* (1×10^7 CFU, n=12 mice per temperature). (G, H) Bacterial CFUs from spleen (G) and liver (H) 1-day post-infection with *E. coli* (1×10^7 CFU, n=9 mice per temperature). (I, J) Plasma triglycerides (I, n=9 mice per temperature) and cytokine concentration (J, n=14 mice per temperature) 1-day post-infection with *E. coli* (1×10^7 CFU). Mean values of cytokines are plotted as a heat map. MCP-1 is higher in mice housed at 22°C ($p<0.05$). (K) Body mass of mice infected with *E. coli* (1×10^8 CFU, n=19 mice per temperature). (L) Kaplan-Meier survival curves of C57BL/6J mice infected with *E. coli* (1×10^8 CFU, n=28–29 mice per temperature; data combined from 3 separate experiments). (M, N) Bacterial CFUs from spleen (M) and liver (N) of C57BL/6J and *Ucp1*$^{-/-}$ mice housed at 22°C and infected with *E. coli* (1×10^7 CFU, n=3–8 mice per genotype and timepoint). (O) Kaplan-Meier survival curves of C57BL/6J and *Ucp1*$^{-/-}$ mice housed at 22°C and infected with *E. coli* (1×10^8 CFU, n=10–14 mice per genotype). (P) Core temperature of C57BL/6J and *Ucp1*$^{-/-}$ mice housed at 22°C and

infected with *E. coli* (1×10^8 CFU, n=10–14 mice per genotype). Data are presented as mean ± SEM. *p < 0.05, **p < 0.01, ***p < 0.001, and ****p <0.0001. See also Figure S7.

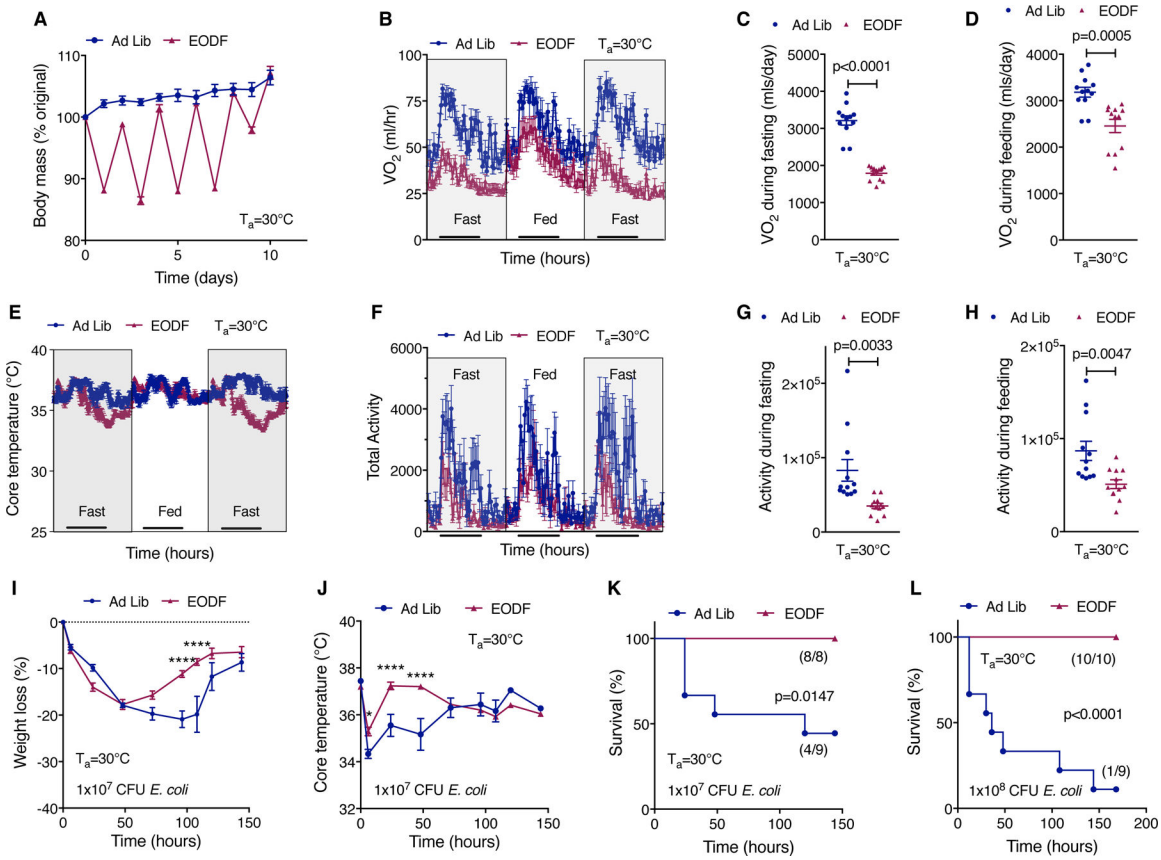

Figure 7. Energy conserving hypometabolic state promotes tolerance during bacterial infection.

(A) Body mass of *ad libitum* (Ad Lib) fed and every other day fasted (EODF) mice housed at 30°C (n=9 mice per condition). (B-D) Rate of oxygen consumption (VO_2) in C57BL/6J mice fed *ad libitum* or subjected to EODF at 30°C (n=6 mice per condition). Total VO_2 consumption during fasting (C) and fed (D) days. (E) Core temperature of C57BL/6J mice housed at 30°C that were fed *ad libitum* (n=3) or subjected to EODF (n=5). (F-H) Total activity in C57BL/6J mice fed *ad libitum* or subjected to EODF at 30°C (n=6 mice per condition). Total activity during fasting (G) and fed (H) days. (I, J) Body mass (I) and core temperature (J) of C57BL/6J mice infected with *E. coli* (1×10^7 CFU) that were fed *ad libitum* (n=9) or previously subjected to 5 cycles of EODF (n=8) at 30°C. (K) Kaplan-Meier survival curves of C57BL/6J mice infected with *E. coli* (1×10^7 CFU) that were fed *ad libitum* (n=9) or previously subjected to 5 cycles of EODF (n=8) at 30°C. (L) Kaplan-Meier survival curves of C57BL/6J mice infected with *E. coli* (1×10^8 CFU) that were fed *ad libitum* (n=9) or previously subjected to 5 cycles of EODF (n=10) at 30°C. See also Figure S7.

KEY RESOURCES TABLE

REAGENT or RESOURCE	SOURCE	IDENTIFIER
Antibodies		
Anti-mouse CD45 (clone 30-F11)	BioLegend	Cat# 103116; RRID: AB_312981
Anti- mouse CD19 (clone 6D5)	BioLegend	Cat# 115509; RRID: AB_313644
Anti- mouse CD5 (clone 53–7.3)	BioLegend	Cat# 100606; RRID: AB_312735
Anti-mouse TLR4 (clone SA15–21)	BioLegend	Cat# 145409; RRID: AB_2566030
Anti-mouse CD11b (clone M1/70)	BioLegend	Cat# 101208; RRID: AB_312791
Anti-mouse F4/80 (clone BM8)	BioLegend	Cat# 123124; RRID: AB_893475
Anti-mouse UQCRC2 (clone 13G12AF12BB11)	abcam	Cat# ab14745; RRID: AB_2213640
Anti-mouse ATP5a	abcam	Cat# ab14748; RRID: AB_301447
Anti-mouse UCP1	abcam	Cat# ab10983; RRID:AB_2241462
Anti-mouse HSP90	Cell Signaling Technology	Cat# 4874S; RRID:AB_2121214
Anti-rabbit MAVS (ubiquitin)	Cell Signaling Technology	Cat# 3933S; RRID: AB_2180538
Anti-rabbit IgG, HRP-conjugated (secondary)	Cell Signaling Technology	Cat# 7074S, RRID:AB_2099233
Streptavidin PECy7	BD Pharmingen	Cat# 557598; RRID: AB_10049577
Bacterial and Virus Strains		
Listeria Monocytogenes Strain: 10403S	From Ari Molofsky, UCSF	N/A
Escherichia coli Strain: O111:B4	From Judith Hellman, UCSF	N/A
Chemicals, Peptides, and Recombinant Proteins		
Lipopolysaccharide (*Escherichia coli O111:B4)* purified by ion-exchange chromatography	Sigma-Aldrich	Cat# L3024
Poly (I:C) - Low Molecular Weight	Invivogen	Cat# tlrl-picw
Heat Killed *Listeria monocytogenes* (HKLM)	Invivogen	Cat# tlrl-hklm
Flagellin (*S. typhimurium*)	Invivogen	Cat# tlrl-stfla
Pam3CSK4	Invivogen	Cat# tlrl-pms
Imiquimod (R837)	Invivogen	Cat# tlrl-imqs
Peptidoglycan (*Bacillus subtilis)*	Sigma-Aldrich	Cat# 69554
ODN 1826 (Class B CpG oligonucleotide)	Invivogen	Cat# tlrl-1826
ODN 1585 (Class A CpG oligonucleotide)	Invivogen	Cat# tlrl-1585

REAGENT or RESOURCE	SOURCE	IDENTIFIER
MG132	Millipore	Cat# 474790
Protease inhibitor cocktail	Sigma-Aldrich	Cat# P8340
Critical Commercial Assays		
Mouse Inflammation CBA kit	BD Biosciences	Cat# 552364
β-Hydroxybutyrate (Ketone Body) Colorimeteric Assay Kit	Cayman Chemical Company	Cat# 700190
Mouse Leptin ELISA Kit	LifeSpan Biosciences	Cat# LS-F269
Triglyceride Colorimetric Assay Kit	Cayman Chemical Company	Cat# 10010303
Rat/Mouse Insulin ELISA	Millipore Sigma	Cat# EZRMI-13K
First Strand cDNA synthesis Kit	Quantabio	Cat# P/N84035
SensiFAST™ SYBR No-Rox	Bioline	Cat# BIO098020
ANGPTL4 ELISA Kit Mouse	abcam	Cat# ab216789
Urea Assay Kit	BioAssay Systems	Cat# DIUR-100
Creatine Kinase Activity Assay Kit (Colorimteric)	abcam	Cat# ab155901
Mouse TNNI3/ Cardiac Troponin I	LifeSpan Biosciences	Cat# LS-F24180
Creatinine (serum) Colorimetric Assay Kit	Cayman Chemical Company	Cat# 700460
NextSeq® 500 Mid Output v2 Kit	Illumina	FC-404–2001
Serum Amyloid A Mouse ELISA Kit	abcam	Cat# ab157723
ProSignal Pico Chemiluminescent Substrate	Prometheus Protein Biology	Cat# 20–300
Deposited Data		
RNA-seq analysis of liver gene expression	https://www.ncbi.nlm.nih.gov/geo/	GSE114473
Experimental Models: Organisms/Strains		
Mouse: C57BL/6J	The Jackson Laboratory	Stock No. 000664
Mouse: Vav1^{cre} (B6.Cg-*Commd10*$^{Tg(Vav1-icre)A2Kio}$/J) (assembled with Tlr4$^{fl/fl}$ and Myd88$^{fl/fl}$)	The Jackson Laboratory	Stock No. 008610

REAGENT or RESOURCE	SOURCE	IDENTIFIER
Mouse: Lyz2^{cre} (B6.129P2-*Lyz2$^{tm1(cre)Ifo}$*/J) (assembled with Tlr4$^{fl/fl}$ and Myd88$^{fl/fl}$)	The Jackson Laboratory	Stock No. 004781
Mouse: Tlr4$^{fl/fl}$ (B6(Cg)-*T lr 4$^{tm1.1Karp}$*/J)	The Jackson Laboratory	Stock No. 024872
Mouse: Myd88$^{fl/fl}$ (B6.129P2(SJL)-*My d 8 8^{tm1Defr}*/J)	The Jackson Laboratory	Stock No. 008888
Mouse: TLR4$^{-/-}$ (B6(Cg)-*T l r 4$^{tm1.2Karp}$*/J)	The Jackson Laboratory	Stock No. 029015
Mouse: MyD88$^{-/-}$ (B6.129P2(SJL)-*My d 8 8$^{tm1.1Defr}$*/J)	The Jackson Laboratory	Stock No. 009088
Mouse: UCP1$^{-/-}$ (*Ucp1^{tm1K}*)	Yuriy Kirichok (PMID: 9139827)	RRID: MGI_1857471
Mouse: Angptl4$^{-/-}$ (*Angptl4^{tm1Jig}*)	Suneil Koliwad (PMID: 15505215)	RRID: MGI_3505565
Oligonucleotides		
Mouse primer: MuRF1 Fwd: 5'GTGTGAGGTGCCTACTTGCTC Rev: 5'GCTCAGTCTTCTGTCCTTGGA	This paper	N/A
Mouse primer: Atrogin1 Fwd: 5'CAGCTTCGTGAGCGACCTC Rev: 5'GGCAGTCGAGAAGTCCAGTC	This paper	N/A
Recombinant DNA		
Software and Algorithms		
Ingenuity Pathway Analysis	Ingenuity Pathway Analysis	https://www.qiagenbioinformatics.com/products/ingenuity-pathway-analysis/
Metascape	Tripathi et al., 2015	http://metascape.org
Kallisto (R)	Bray et al., 2016	https://pachterlab.github.io/kallisto/
Sleuth (R)	Pimentel et al., 2017	https://pachterlab.github.io/sleuth/
Trimmomatic	Bolger et. al., 2014	http://www.usadellab.org/cms/?page=trimmomatic
Agilent MassHunter Quant B.07.00.	Agilent	https://www.agilent.com/en/products/software-informatics/masshunter-suite/masshunter/masshunter-software
Prism 7.0	Graphpad	https://www.graphpad.com/scientific-software/prism/

REAGENT or RESOURCE	SOURCE	IDENTIFIER
Other		
Rectal Probe Thermometer	PhysiTemp	BAT-12 Microprobe
E-mitter Mouse Telemetry System	Starr Life Sciences Corp.	G2 E-mitter
CLAMS	Columbus Instruments	N/A
Clark-type Oxygen Electrode	Strathkelvin Instruments	Model 782/MT200
Infrared Thermography	FLIR	FLIR E60